aerospace

MDPI

Article

Real-Time Surface Temperature Reconstruction of Thermal Protection Structures via Deep-Embedded Sensors Without Explicit Thermophysical-Property Information

Bocheng Sun [1], Xiangyu Wei [1], Pengyu Nan [1,2], Guoguo Xin [1,2] and Hangzhou Yang [1,2,*]

[1] School of Physics, Northwest University, Xi'an 710127, China; 1305561101x@gmail.com (B.S.); wxy19950224@126.com (X.W.); nwu_npy@nwu.edu.cn (P.N.); xinguo@nwu.edu.cn (G.X.)
[2] Fundamental Discipline Research Center for Quantum Science and Technology of Shaanxi Province, Xi'an 710127, China
* Correspondence: yanghz@nwu.edu.cn

Abstract

Monitoring the surface thermal state of thermal protection structures (TPS) is essential for the safe operation and health assessment of hypersonic vehicles. However, direct sensor deployment on heated surfaces suffers from poor survivability, while many model-based approaches require prescribed thermophysical properties and boundary conditions. This study proposes an AutoRegressive with eXogenous input (ARX)-based surface temperature reconstruction method using deep-embedded sensors. By identifying a local equivalent dynamic mapping among internal temperature responses, the method reconstructs the near-surface temperature through virtual-point recursive extrapolation without requiring explicit thermophysical-property or boundary-condition information. Numerical simulations show high accuracy under adiabatic, natural-convection, and forced-convection rear-surface boundaries, with the global RRMSE remaining within 1.09%. Further analyses demonstrate tolerance to moderate temperature- and space-dependent variations in equivalent thermophysical properties; simulations using realistic LI-900 thermal conductivity variations confirm its applicability under different effective conductivity conditions. Single-sided heating experiments with two sensor-embedding layouts validate the method, yielding RRMSE values of 1.74% for the 5-point model and 4.27% for the 9-point model in the main validation case. The applicable conditions are further clarified through analyses of internal temperature-difference SNR, recursive error accumulation, and sensor-layout constraints. The proposed method provides a low-cost and long-life solution for online TPS surface temperature monitoring.

Keywords: thermal protection system; thermal identification; surface temperature reconstruction; deep-embedded sensors; autoregressive with exogenous input

Check for updates

Academic Editors: Kyun Ho Lee and Hossein Zare-Behtash

Received: 5 June 2026
Revised: 15 July 2026
Accepted: 28 July 2026
Published: 1 August 2026

Copyright: © 2026 by the authors. Licensee MDPI, Basel, Switzerland. This article is an open access article distributed under the terms and conditions of the Creative Commons Attribution (CC BY) license.

1. Introduction

Reusable launch vehicles represent a pivotal development direction for future space transportation systems, possessing the capability for multiple round trips between the Earth's atmosphere and low Earth orbit. Their core advantage lies in their ability to return safely upon mission completion and be redeployed for subsequent launches following localized maintenance and inspection. This characteristic is of profound strategic significance for drastically reducing launch costs and increasing the frequency of space access [1–3].

During hypersonic flight, intense aerodynamic compression and surface friction subject the vehicle to exceptionally severe transient aerodynamic heating loads. Consequently, the fuselage shell is exposed to extreme physical environments, including high-temperature shock waves and strong oxidation, which severely threaten the structural integrity of the vehicle and the normal operation of its internal systems [4–7]. As the primary physical barrier against these extreme conditions, the thermal protection structure (TPS) directly determines the vehicle's survivability and service life. Accurately obtaining the transient temperature evolution on the outer surface of the TPS during its service is crucial for evaluating its thermal insulation efficacy and structural health. It also serves as an essential theoretical basis for guiding the structural optimization of the TPS, achieving a unified balance between thermal protection and weight reduction, and establishing scientific maintenance cycles [8–12].

However, constrained by harsh surface conditions—such as extreme heat fluxes, material ablation, and severe aerodynamic scouring—direct and precise measurement of the transient temperature on the windward surface of the TPS using traditional sensors presents significant engineering challenges and severely compromises sensor survivability. Therefore, the prevailing engineering alternative involves embedding temperature sensors within the internal structure of the TPS to collect discrete, attenuated internal temperature responses, which are then used to inversely reconstruct the surface thermal boundary conditions. This type of indirect reconstruction is closely related to inverse heat-conduction analysis, where internal or accessible temperature observations are used to infer inaccessible thermal boundary information [13–15]. Its practical difficulty lies in obtaining stable and accurate reconstruction from limited internal measurements under uncertain material and boundary conditions.

For indirect thermal-boundary reconstruction, inverse heat-conduction analysis has provided many useful numerical tools, including analytical methods, gradient-based optimization, stochastic inference, and regularization techniques [16,17]. Among them, gradient-based methods have been widely used because of their computational efficiency and clear optimization framework. For example, Pandey et al. [18] combined the sequential function specification method with the conjugate gradient method for simultaneous multi-parameter inversion, and Cui et al. [19] coupled gradient optimization with finite element analysis to identify thermal loads in scramjet combustor structures. In addition, Khosravi et al. [20] coupled the Levenberg–Marquardt algorithm with a computational fluid dynamics solver for sparse-measurement thermal-boundary reconstruction, whereas Sajedi et al. [21] enhanced the noise robustness of LM-based inversion through adaptive damping-factor adjustment.

With the development of computational techniques, stochastic inference, swarm intelligence, and physics-informed learning have also been introduced into indirect thermal-state reconstruction. For example, Bayesian and Markov-chain Monte Carlo methods have been used to estimate inaccessible heat-transfer coefficients with uncertainty quantification [22], while Kalman filter-based and weighted recursive least squares approaches have been applied to reconstruct moving heat sources and transient temperature fields [23]. More recently, data-driven and physics-informed frameworks have shown strong potential for TPS-related thermal-field reconstruction. Wei et al. [24,25] developed learning-based and mesh-free reconstruction frameworks for three-dimensional transient temperature and thermomechanical fields of hypersonic vehicle TPS; PINN-based methods have been widely explored for sparse-data thermal and flow-field reconstruction [26–30]. Liu et al. [31] further improved the robustness and training efficiency of PINNs by introducing a cooperative soft–hard constraint strategy.

Because indirect thermal reconstruction is often sensitive to measurement noise, regularization techniques have also been widely incorporated into thermal-boundary reconstruction frameworks to improve solution stability [32,33]. For example, Tikhonov regularization has been combined with evolutionary optimization to balance reconstruction accuracy and noise robustness [34], while total-variation regularization has been introduced to preserve abrupt heat-flux variations during boundary estimation [35].

Although the above methods have achieved remarkable progress, many model-based inversion frameworks still require prescribed thermophysical properties, detailed boundary conditions, and repeated forward-model evaluations. For TPS materials operating under high-temperature and long-duration service environments, the effective thermal response may vary with temperature, aging, moisture exposure, damage accumulation, or microstructural evolution. These uncertainties increase the difficulty of directly applying conventional inversion models in real-time monitoring scenarios.

To reduce the dependence on prescribed thermophysical inputs while retaining the basic heat-transfer mechanism, system identification provides an alternative strategy for constructing equivalent dynamic relationships from measured temperature responses. Among such techniques, the AutoRegressive with eXogenous input (ARX) model is a classical time-series identification method and has been applied in various thermal systems, including temperature prediction in slab reheating furnaces [36], thermal deformation compensation in machining processes [37], measurement-delay correction for thermocouples and fiber Bragg grating sensors [38–40], and indoor thermal-dynamics prediction in buildings [41]. These studies indicate that ARX-type models can effectively characterize dynamic thermal transfer relationships from measured data. This provides a useful basis for constructing a local equivalent mapping between deep-embedded sensor responses and near-surface temperature, without explicitly identifying temperature-dependent thermophysical property functions.

To address the key engineering challenges of low sensor survivability under extreme thermal loads and the strong dependence of conventional temperature reconstruction methods on prescribed thermophysical properties and boundary conditions, this paper proposes a surface temperature reconstruction method based on deep-embedded sensors. Based on the one-dimensional Fourier heat-conduction relationship, the proposed method identifies a local equivalent dynamic mapping among temperature responses at different depths and reconstructs the near-surface temperature through virtual-point recursive extrapolation. Its core advantage lies not only in estimating the surface thermal state without requiring explicit real-time thermophysical-property functions or boundary-condition information, but also in enabling temperature sensors to be embedded in deeper measurement regions away from the extremely hot surface. This feature significantly reduces the risk of sensor failure in high-temperature environments and improves the durability of the measurement system. Therefore, the proposed method is expected to provide a low-cost and long-life solution for the online monitoring of extreme surface temperature fields in hypersonic vehicles.

2. Methodology

2.1. Physical Model and Equation Reconstruction

The quasi-one-dimensional model adopted in this study is not intended to describe the global aerothermal heat-flux distribution over the entire windward surface of a flight vehicle. Instead, it is applied to representative core regions of large-area TPS that are sufficiently far from leading edges, gaps, joints, heat-short paths, and other strong three-dimensional disturbance regions. In these regions, heat transfer is mainly dominated by the through-thickness direction, while lateral heat conduction and edge effects are relatively weak. Therefore, the local thermal response can be approximated as a quasi one-dimensional transient heat-

conduction process. Similar one-dimensional treatments have also been adopted in multilayer TPS thermal-response and aerothermal-heating reconstruction studies [42,43]. Within this scope, the quasi one-dimensional formulation reduces model complexity and computational cost, enabling efficient ARX parameter identification and virtual-point recursive extrapolation for real-time surface-temperature reconstruction.

Figure 1a illustrates a quasi one-dimensional heat conduction process within a structure. One side of the structure ($x = 0$) is defined as the heated surface, which directly bears the external aerodynamic heating load; its surface temperature is denoted as the heat source temperature T_S. The other side ($x = x_0$) serves as a free boundary subjected to mixed heat transfer conditions, defined as $q = f(T)$. Along the thickness direction of the structure, three temperature measurement points, denoted as A, B, and C, are sequentially arranged along the positive x-axis.

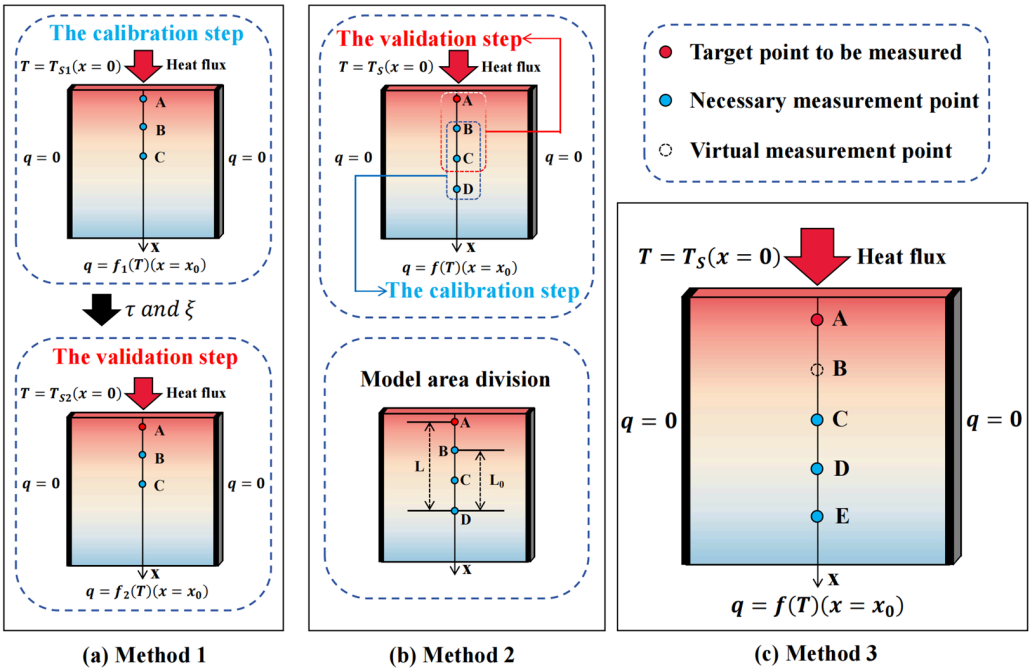


Figure 1. Schematics of three ARX-based surface temperature reconstruction strategies: (**a**) method 1: utilizing independent prior calibration to derive parameters for subsequent reconstruction; (**b**) method 2: integrating calibration and validation processes with model regional division; and (**c**) method 3: introducing virtual point B for layer-by-layer recursive reconstruction to minimize the measurement zone ratio.

In the Cartesian coordinate system, the governing equation for this one-dimensional transient heat-conduction process can be described by Fourier's law as [44]:

$$\rho c \frac{\partial T}{\partial t} = k \frac{\partial^2 T}{\partial x^2} \tag{1}$$

where ρ, c, and k denote the effective density, effective specific heat capacity, and effective thermal conductivity of the material, respectively. In practical TPS materials, these thermophysical properties may vary with temperature during heating. Therefore, in the following derivation, ρ, c, and k should be interpreted as local equivalent thermophysical parameters within the small spatial region considered in the discrete heat-transfer relationship, rather than as globally constant material properties over the entire structure and the whole heating process.

To establish numerical correlations among the temperature responses of the internal measurement points, the finite difference method is employed to discretize Equation (1).

Focusing on the central point B, spatial discretization is performed using a non-uniform grid template, yielding the following expression:

$$\rho c \frac{\partial T_B}{\partial t} = 2k \frac{\left(\frac{T_C - T_B}{x_C - x_B} - \frac{T_B - T_A}{x_B - x_A}\right)}{(x_C - x_B) + (x_B - x_A)} \tag{2}$$

where T_A, T_B, and T_C denote the transient temperature measurements of the corresponding points. Notably, point A is situated closest to the heated surface, enabling its temperature T_A to adequately represent the heat source temperature. The variables x_A, x_B, and x_C represent the vertical depths of the respective measurement points relative to the heated surface.

By rearranging Equation (2), it can be further expressed as:

$$T_A = \frac{\rho c}{2k}(x_B - x_A)(x_C - x_A)\frac{\partial T_B}{\partial t} + \left(1 + \frac{x_B - x_A}{x_C - x_B}\right)T_B - \frac{x_B - x_A}{x_C - x_B}T_C \tag{3}$$

To elucidate the mathematical features of this physical process and simplify the model structure, the above equation can be integrated and simplified as follows:

$$\begin{aligned} T_A &= \tau \frac{\partial T_B}{\partial t} + (1 + \xi)T_B - \xi T_C \\ \tau &= \frac{\rho c}{2k} x_{AB} x_{AC} \\ \xi &= \frac{x_{AB}}{x_{BC}} \end{aligned} \tag{4}$$

Equation (4) establishes the physical constraint relationship among the temperature fields of the three internal measurement points. Here, x_{AB} denotes the distance between points A and B, x_{BC} denotes the distance between points B and C, and x_{AC} denotes the distance between points A and C. τ is termed the characteristic time constant, which is jointly determined by the material's thermophysical properties and the spatial locations of the measurement points. It characterizes the thermal inertia and time-delay effects during the heat-conduction process from point A to point B. ξ is termed the geometric thermal resistance ratio, which is numerically equal to the ratio of x_{AB} to x_{BC}. Physically, it reflects the proportional relationship of thermal conduction resistances between different measurement zones within the structure.

Theoretically, provided that the characteristic parameters τ and ξ are known, the temperature at point A—namely, the heat source temperature—can be directly reconstructed utilizing the transient temperature responses of points B and C. However, under realistic hypersonic flight conditions, the precise real-time distribution of the material's effective thermophysical parameters (ρ, c, and k) is notoriously difficult to acquire in extreme environments. As a result, the true values of τ and ξ cannot be directly determined via analytical calculations.

To overcome the reconstruction difficulties arising from the uncertainty of thermophysical properties, the ARX method is introduced to solve for the parameters. The differential term in Equation (4) is discretized in the time domain and transformed into a matrix form suitable for least squares estimation:

$$\mathbf{A} = \mathbf{B}\mathbf{X} \tag{5}$$

where:

$$\mathbf{A} = \left[(T_A)_{t=t_0}, (T_A)_{t=2t_0}, \cdots, (T_A)_{t=Nt_0}\right]^{\mathrm{T}} \tag{6}$$

$$\mathbf{B} = \begin{bmatrix} \left.\frac{\partial T_B}{\partial t}\right|_{t=t_0} & (T_B)_{t=t_0} & (T_C)_{t=t_0} \\ \left.\frac{\partial T_B}{\partial t}\right|_{t=2t_0} & (T_B)_{t=2t_0} & (T_C)_{t=2t_0} \\ \vdots & \vdots & \vdots \\ \left.\frac{\partial T_B}{\partial t}\right|_{t=Nt_0} & (T_B)_{t=Nt_0} & (T_C)_{t=Nt_0} \end{bmatrix} \tag{7}$$

X is termed the parameter matrix, with its content defined as:

$$\mathbf{X} = [\tau, 1+\xi, -\xi]^{\mathrm{T}} \tag{8}$$

the matrix **X** can be solved using the least squares method:

$$\mathbf{X} = (\mathbf{B}^{\mathrm{T}}\mathbf{B})^{-1}\mathbf{B}^{\mathrm{T}}\mathbf{A} \tag{9}$$

For the finite-dimensional least squares problem in Equation (9), the parameter solution is unique when the regression matrix **B** has full column rank, i.e., rank(**B**) $= n_X$, because $\mathbf{B}^{\mathrm{T}}\mathbf{B}$ is then nonsingular. This condition is numerically verified using the experimental datasets in Appendix G.

Through the above equation, the numerical values of the parameters τ and ξ can be determined without requiring prior knowledge of the structure's thermophysical properties. Subsequently, the temperature at point A can be estimated by combining these parameters with the temperature measurement data from points B and C.

2.2. Temperature Field Calibration and Reconstruction

As illustrated in Figure 1a, Method 1 divides the reconstruction process into a calibration phase and a validation phase. During the calibration phase, the heated surface temperature of the structure is $T = T_{S1}$, the free boundary heat flux is $q = f_1(T)$, and the lateral walls are considered adiabatic. Temperature sensors are employed to acquire the transient responses at points A, B, and C. By substituting these data into Equations (6)–(9), the characteristic parameters τ and ξ corresponding to the structure can be resolved. In the validation phase, where the heated surface temperature is $T = T_{S2}$ and the free boundary heat flux is $q = f_2(T)$, the temperature at point A can be reconstructed by substituting the temperature data solely from points B and C, along with the predetermined τ and ξ from the calibration phase, into Equation (4).

Although Method 1 is logically clear and intuitive, it exhibits two prominent limitations in practical engineering applications. First, the step-by-step implementation increases the complexity and time cost of experimental operations. Second, it is highly challenging to strictly ensure the consistency of sensor installation positions and thermal contact resistances between the calibration experiment and actual service conditions, which may introduce additional systematic errors.

Method 2 is proposed as an advancement over Method 1. As depicted in Figure 1b, the calibration and validation processes can be integrated concurrently to mitigate the discrepancies caused by independent sensor deployments across separate phases. By introducing a fourth measurement point, D, the ARX solution matrix is constructed using three consecutive deeper measurement points (B, C, and D). Assuming that the thermophysical properties of the structural material are locally uniform, the transfer characteristic parameters of the B-C-D subsystem can be considered approximately equivalent to, or having a deterministic mapping relationship with, those of the A-B-C subsystem. Consequently, the system parameter matrix **X** can be identified using the temperature data from points B, C, and D. By combining this matrix with the temperature measurements from points B and

C, the temperature at point A can be directly reconstructed via Equation (4). This process entirely eliminates the reliance on actual measured data at point A.

To quantify the impact of sensor deployment depth on reconstruction performance, the following geometric definitions are introduced: the total experimental zone depth, L, refers to the vertical distance from the deepest sensor (e.g., point D) to the heated surface (represented by point A); the measurement zone depth, L_0, denotes the spatial span of the actually deployed sensors, i.e., the distance between the shallowest and the deepest sensors; the measurement zone ratio is defined as $d = L_0/L$. For instance, in Figure 1b, $d = 2/3$. In engineering practice, a smaller d indicates that the entire sensor array is positioned further away from the heated surface. This not only places the sensors in a milder thermal environment—thereby significantly lowering the manufacturing requirements for high-temperature resistance and extending their service life—but also mitigates potential disturbances to the aerodynamic contour near the structural wall.

To further push the measurement zone into the deep layers of the structure (i.e., to further reduce the value of d), an iterative extrapolation strategy introducing a virtual point is proposed built upon Method 2, which corresponds to Method 3, as shown in Figure 1c.

This model involves five spatial points: A, B, C, D, and E. Among them, C, D, and E represent physical measurement points where sensors are actually deployed, whereas A and B denote unknown points to be solved. Because point B lacks actual measured data yet serves as an intermediate variable for reconstructing point A, it is termed a virtual point. Since the temperature data of five locations (A, B, C, D, and E) are collectively involved, this framework is referred to as the 5-point model.

Focusing initially on the deepest subsystem, C-D-E, the observation vector $\mathbf{A}_{CDE}$ and the regression matrix $\mathbf{B}_{CDE}$ are constructed utilizing the measured transient temperature series from points C, D, and E to solve for the coefficient matrix $\mathbf{X}_{CDE}$ of this sub-region:

$$\mathbf{X}_{CDE} = (\mathbf{B}_{CDE}{}^{\mathrm{T}}\mathbf{B}_{CDE})^{-1}\mathbf{B}_{CDE}{}^{\mathrm{T}}\mathbf{A}_{CDE} \tag{10}$$

$$\mathbf{A}_{CDE} = \left[(T_C)_{t=t_0}, (T_C)_{t=2t_0}, \cdots, (T_C)_{t=Nt_0}\right]^{\mathrm{T}} \tag{11}$$

$$\mathbf{B}_{CDE} = \begin{bmatrix} \left.\frac{\partial T_D}{\partial t}\right|_{t=t_0} & (T_D)_{t=t_0} & (T_E)_{t=t_0} \\ \left.\frac{\partial T_D}{\partial t}\right|_{t=2t_0} & (T_D)_{t=2t_0} & (T_E)_{t=2t_0} \\ \vdots & \vdots & \vdots \\ \left.\frac{\partial T_D}{\partial t}\right|_{t=Nt_0} & (T_D)_{t=Nt_0} & (T_E)_{t=Nt_0} \end{bmatrix} \tag{12}$$

The corresponding parameter matrix encapsulates the local thermal characteristics of the C-D-E region:

$$\mathbf{X}_{CDE} = \left[\tau', 1+\xi', -\xi'\right]^{\mathrm{T}} \tag{13}$$

To facilitate the upward propagation of thermal information, a spatial invariance assumption must be introduced. Specifically, under the premise of uniform grid spacing and locally homogeneous material thermophysical properties, the transfer matrices of adjacent sub-regions are numerically approximately equivalent, i.e., $\mathbf{X}_{CDE} \approx \mathbf{X}_{BCD} \approx \mathbf{X}_{ABC}$. Consequently, $\mathbf{X}_{CDE}$ can serve directly as an approximate surrogate for $\mathbf{X}_{BCD}$. By combining this with the regression matrix $\mathbf{B}_{BCD}$ of the B-C-D subsystem, the temperature of the virtual point B, denoted as T_B, can be deduced:

$$\mathbf{A}_{BCD} = \left[(T_B)_{t=t_0}, (T_B)_{t=2t_0}, \cdots, (T_B)_{t=Nt_0}\right]^{\mathrm{T}} \tag{14}$$

$$\mathbf{B}_{BCD} = \begin{bmatrix} \left.\frac{\partial T_C}{\partial t}\right|_{t=t_0} & (T_C)_{t=t_0} & (T_D)_{t=t_0} \\ \left.\frac{\partial T_C}{\partial t}\right|_{t=2t_0} & (T_C)_{t=2t_0} & (T_D)_{t=2t_0} \\ \vdots & \vdots & \vdots \\ \left.\frac{\partial T_C}{\partial t}\right|_{t=Nt_0} & (T_C)_{t=Nt_0} & (T_D)_{t=Nt_0} \end{bmatrix} \tag{15}$$

$$\mathbf{A}_{BCD} = \mathbf{B}_{BCD}\mathbf{X}_{BCD} \approx \mathbf{B}_{BCD}\mathbf{X}_{CDE} \tag{16}$$

$$T_B = \tau' \frac{\partial T_C}{\partial t} + (1+\xi')T_C - \xi' T_D \tag{17}$$

Once the reconstructed temperature data for the virtual point B are obtained, the aforementioned recursive process is repeated. The regression matrix $\mathbf{B}_{ABC}$ is constructed utilizing the data from the measured point C and the reconstructed point B. By reapplying the parameter matrix $\mathbf{X}_{CDE}$, the temperature of the target point A is ultimately resolved:

$$\mathbf{A}_{ABC} = [(T_A)_{t=t_0}, (T_A)_{t=2t_0}, \cdots, (T_A)_{t=Nt_0}]^{\mathrm{T}} \tag{18}$$

$$\mathbf{B}_{ABC} = \begin{bmatrix} \left.\frac{\partial T_B}{\partial t}\right|_{t=t_0} & (T_B)_{t=t_0} & (T_C)_{t=t_0} \\ \left.\frac{\partial T_B}{\partial t}\right|_{t=2t_0} & (T_B)_{t=2t_0} & (T_C)_{t=2t_0} \\ \vdots & \vdots & \vdots \\ \left.\frac{\partial T_B}{\partial t}\right|_{t=Nt_0} & (T_B)_{t=Nt_0} & (T_C)_{t=Nt_0} \end{bmatrix} \tag{19}$$

$$\mathbf{A}_{ABC} = \mathbf{B}_{ABC}\mathbf{X}_{ABC} \approx \mathbf{B}_{ABC}\mathbf{X}_{CDE} \tag{20}$$

$$T_A = \tau' \frac{\partial T_B}{\partial t} + (1+\xi')T_B - \xi' T_C \tag{21}$$

By introducing the virtual point, Method 3 successfully reduces d to 1/2, enabling the sensor array to be positioned further away from the high-temperature aerodynamic heating surface, thereby significantly enhancing the survivability of the measurement system. However, it must be emphasized that the validity of this method is predicated on a strict geometric constraint: the five measurement points (A, B, C, D, and E) must be equally spaced along the depth direction. This constraint serves as a necessary and sufficient condition to ensure the accuracy of the central difference approximation for the second-order partial derivative in the finite difference scheme and to guarantee the numerical consistency among the system parameter matrices ($\mathbf{X}_{ABC}$, $\mathbf{X}_{BCD}$, and $\mathbf{X}_{CDE}$) of the respective sub-regions. The feasibility of Method 3 is further evaluated through numerical simulations and experimental validations in Sections 3 and 4, respectively, while its applicable conditions and limitations are discussed in Section 5.

3. Numerical Simulation

3.1. Verification of Method Applicability Under Various Boundary Conditions

To comprehensively verify the theoretical feasibility and environmental adaptability of the proposed Method 3 under complex thermal environments, a quasi one-dimensional transient heat-conduction finite element model was established using COMSOL Multiphysics 6.1, as depicted in Figure 2.

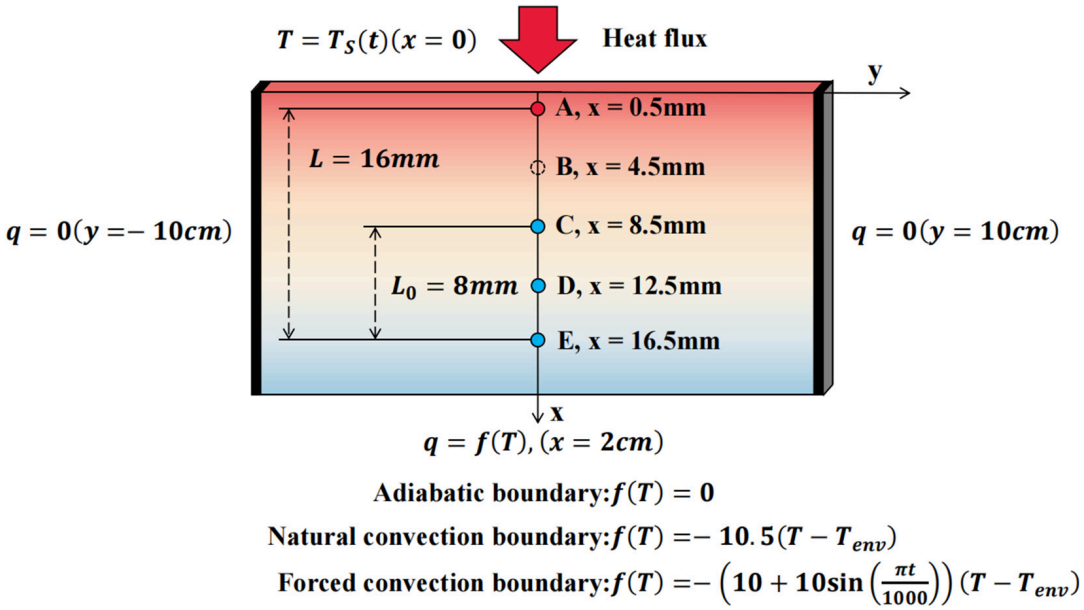


Figure 2. Schematic of the quasi-one-dimensional heat conduction model under single-sided heating.

To simulate a realistic and harsh aerodynamic heating environment, a time-varying temperature boundary condition, $T_S(t)$, as illustrated in Figure 3, was applied to the heated surface (x = 0). This heating curve comprises three typical phases. During the ascending phase, the temperature initiates from the ambient temperature T_{env} (298.15 K) and undergoes eight successive heating-and-dwelling cycles; each step involves a 2 min temperature ramp followed by a 5 min isothermal dwell. Upon reaching the peak temperature of 1498.15 K (1225 °C), the temperature is maintained constant for 15 min before initiating the cooling phase. To verify the adaptability of the algorithm to unknown rear-surface environments, three distinctly different boundary conditions were established on the cooling surface of the model (x = 2 cm): an adiabatic boundary ($q = 0$), a natural convection boundary ($q = -10.5(x - T_{\text{env}})$), and a forced convection boundary ($q = -(10 + 10\sin(\pi t/1000))(x - T_{\text{env}})$). Additionally, both lateral walls of the model (y = ±10 cm) were set as adiabatic boundaries. In Figure 2, point A is not placed exactly on the heated surface, but is instead located at a depth of 0.5 mm. In the actual experiment, to ensure uniform contact between the specimen and the heating stage, the reference thermocouple used to measure the heated surface temperature cannot be directly placed on the contact surface and can only be embedded adjacent to the heated surface. The small depth of 0.5 mm is used to minimize the deviation from the prescribed surface-temperature boundary while maintaining consistency with the practical embedded-sensor arrangement.

In the simulation setup, the material utilized for the structure possesses a density of ρ_0 = 144 kg/m^3, a thermal conductivity of k_0 = 0.0795 W/(m·K), and a specific heat capacity of c_0 = 1260 J/(kg·K). The total depth of the experimental zone is L = 16 mm and a representative sensor spacing of 4 mm is selected. This spacing places the actual measurement points relatively far from the heated surface, thereby producing more pronounced thermal attenuation and response delay during heat transfer. Such a configuration is used to simulate the weakened thermal information received by deeply embedded sensors and to evaluate whether the proposed method can reconstruct the heated-surface temperature from attenuated internal temperature responses.

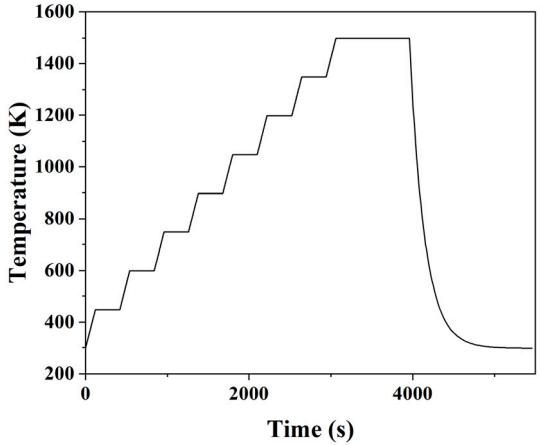


Figure 3. The prescribed step-like time-varying temperature load curve on the heated surface.

To evaluate the capability of Method 3 in reconstructing surface temperatures from deeply embedded sensors, this simulation predominantly investigates the influence of d on reconstruction accuracy. Under the premise of maintaining a constant total experimental zone depth L, the measurement zone depth L_0 is compressed by altering the spatial density of the internal measurement points (C, D, and E). Consequently, simulation groups with varying values of d are constructed to verify the reconstruction efficacy of the proposed method when sensors are positioned further away from the heated surface.

Using the 5-point model with a measurement zone ratio of $d = 1/2$ (as depicted in Figure 2) as a representative case, this section comparatively analyzes the fitting results under three typical operating conditions: adiabatic, natural convection, and forced convection. Figure 4 displays the temperature evolution curves of each measurement point (A, B, C, D, and E) across the complete temperature-varying process, with total simulation durations of 6500 s for the adiabatic case and 5500 s for the natural- and forced-convection cases. The longer duration for the adiabatic case is used to capture its slower cooling process. Because point A is located near the heated surface and is mainly governed by the prescribed temperature boundary, its temperature histories under the three cold-side boundary conditions almost overlap. In contrast, the deeper measurement points are affected more evidently by the cooling-surface boundary; however, this influence appears with a clear thermal delay.

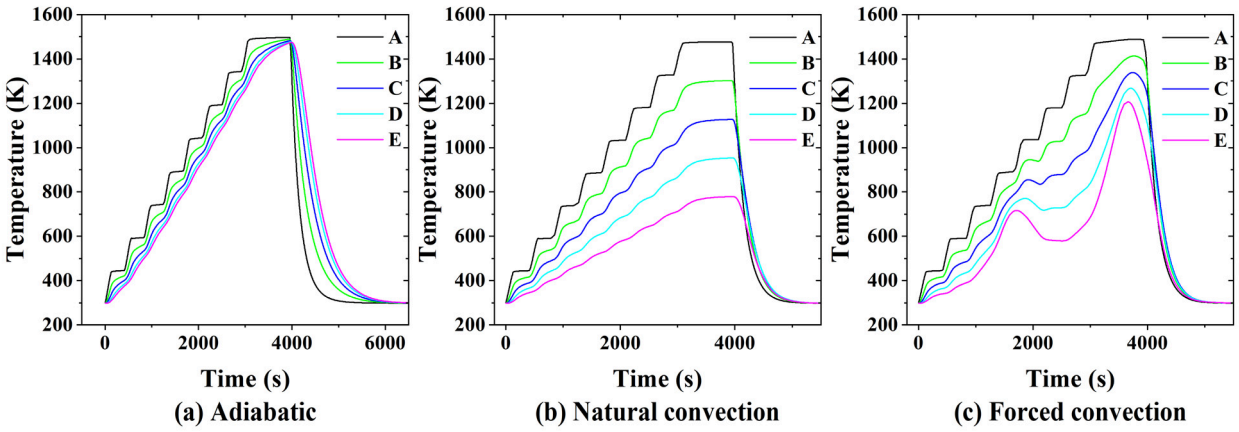


Figure 4. Transient temperature response curves of internal measurement points under different cooling surface boundary conditions.

Under the adiabatic condition, heat cannot dissipate through the rear surface, leading to heat accumulation inside the structure and a slow cooling response of the deep measurement points. Under natural convection, rear-surface heat dissipation reduces the peak

temperatures of the internal points and slightly accelerates the cooling process. Under forced convection, the fluctuating cold-side boundary further affects the deep temperature responses, especially at point E, where obvious oscillations and faster cooling can be observed.

The theory enabling the iterative reconstruction of Method 3 is founded on the assumption of spatial consistency of parameters. To verify the validity of this core assumption, the system parameters τ and ξ, identified in each sub-region under the three boundary conditions, were calculated and their statistical results are presented in Figure 5. Figure 5 illustrates the distribution of τ and ξ across different spatial locations and operating conditions in the form of mean $\pm$ standard deviation. To quantify the relative spatial variation of the identified parameters, the relative standard deviation (RSD) is introduced as:

$$\mathrm{RSD} = \frac{\sqrt{\frac{1}{n}\sum_{i=1}^{n}(x_i - \overline{x})^2}}{\overline{x}} \times 100\% \tag{22}$$

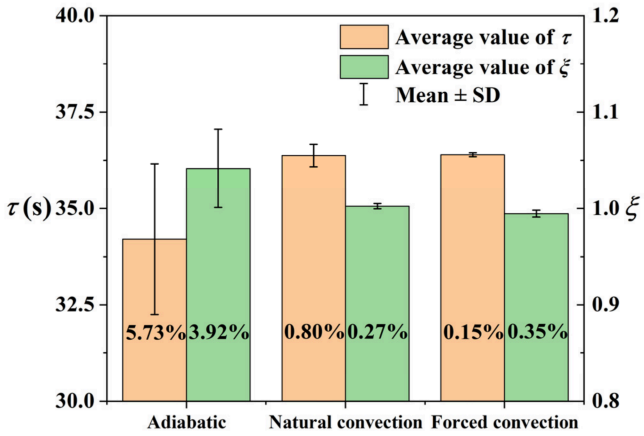


Figure 5. Spatial consistency statistics of the system characteristic parameters τ and ξ.

This value is annotated within each bar in Figure 5. Here, x_i denotes the i-th identified parameter value within different sub-regions, $\overline{x}$ is the mean value, and n is the number of samples. The results show that the identified parameters remain highly consistent across adjacent sub-regions under different boundary conditions. Under natural- and forced-convection conditions, the RSDs of τ and ξ are very low, with $\tau < 0.8\%$ and $\xi < 0.35\%$, indicating the strong spatial consistency of the ARX parameter matrices. Under the adiabatic condition, the RSDs increase slightly to approximately 5.73% for τ and 3.92% for ξ. This increase is mainly attributed to the weaker through-thickness temperature differences during the late thermal response, which makes the identified parameters more sensitive to small numerical and measurement perturbations. Nevertheless, the overall variation remains limited and does not significantly affect the final reconstruction accuracy. Therefore, the results in Figure 5 support the spatial-consistency assumption required for virtual-point recursive extrapolation under the tested boundary conditions.

To quantitatively evaluate the reconstruction performance of Method 3 under different thermal boundary conditions, the reconstructed temperature at point A, denoted as RA in Figure 6 and expressed as $\widehat{T_A}$ in the following formulas, was compared with the reference temperature T_A obtained from the finite element simulation. The instantaneous relative error (RE), used to describe the time-resolved deviation between $\widehat{T_A}$ and T_A, is defined as:

$$\mathrm{RE}(t) = \frac{\left|\widehat{T_A}(t) - T_A(t)\right|}{T_A(t)} \times 100\% \tag{23}$$

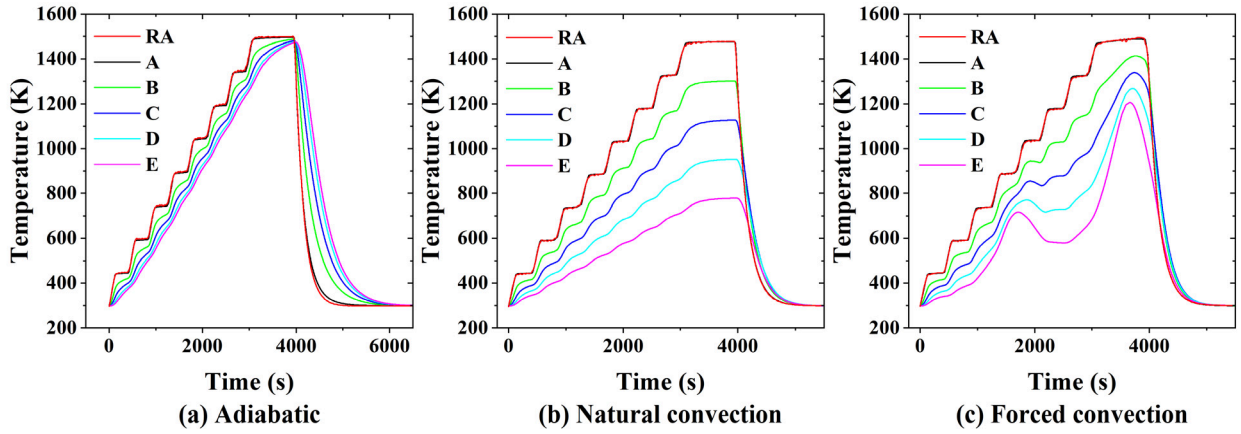


Figure 6. Reconstructed results of point A under different boundary conditions.

Furthermore, the relative root mean square error (RRMSE) is introduced as a global metric to evaluate the overall accuracy across the entire time domain:

$$\mathrm{RRMSE} = \frac{\sqrt{\frac{1}{n}\sum_{i=1}^{n}\left[\widehat{T_A}(t_i) - T_A(t_i)\right]^2}}{\overline{T_A}} \times 100\% \tag{24}$$

where $T_A(t_i)$ and $\widehat{T_A}(t_i)$ denote the reference and reconstructed temperatures at point A at time t_i, respectively; n is the number of time samples; and $\overline{T_A}$ is the time-averaged reference temperature at point A.

As shown in Figures 6 and 7, during the multi-stage step-heating and high-temperature dwell phases from 0 to 4000 s, the reconstructed temperatures under the three cold-side boundary conditions are all in good agreement with the reference temperatures. The instantaneous relative error is generally below 2%, indicating that the proposed virtual-point recursive extrapolation method can effectively capture the transient temperature response during rapid heating and step changes.

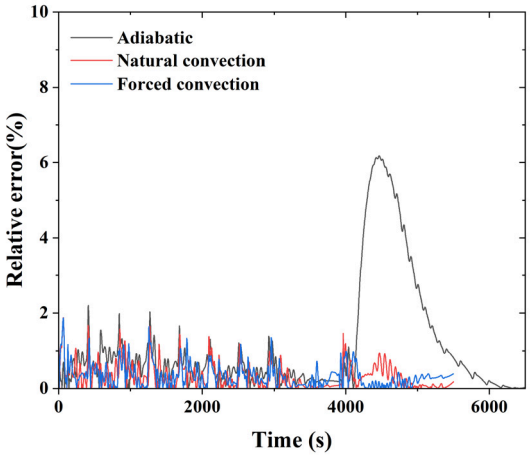


Figure 7. Instantaneous relative error curves under different boundary conditions.

After entering the rapid cooling stage at t > 4000 s, the reconstruction behavior becomes more dependent on the cold-side boundary condition. Under natural- and forced-convection conditions, the reconstructed curves remain highly consistent with the reference curves, and the relative error remains low during cooling. In contrast, under the adiabatic condition, a transient lagging deviation appears at the initial cooling stage and the maximum instantaneous relative error reaches 6.18%. This error increase is mainly asso-

ciated with the evolution of the through-thickness temperature gradient. Although the near-surface temperature histories under different cold-side boundary conditions show similar cooling trends, their internal temperature distributions are different. As illustrated in Appendix A, Figure A1, the adiabatic rear boundary causes the deeper region to retain stored heat for a longer time, producing a temporary mismatch between rapid near-surface cooling and delayed internal thermal response. Rear-surface convection, by contrast, helps to maintain clearer through-thickness temperature differences and provides more effective differential information for ARX parameter identification during cooling.

Across the entire time domain, the RRMSE values are 1.09%, 0.45%, and 0.46% for the adiabatic, natural-convection, and forced-convection cases, respectively. Although a localized error increase occurs during adiabatic cooling, the global error remains approximately 1.1%, indicating that Method 3 maintains high reconstruction accuracy under the tested boundary conditions.

3.2. Verification of Method Applicability Under Different Measurement Zone Ratios

To further explore the applicability of Method 3 in deep measurement scenarios, this section investigates the effect of the measurement zone ratio d on reconstruction accuracy. With the total experimental zone depth L kept constant, the original 5-point model ($d = 1/2$) is extended to 9-point ($d = 1/4$) and 17-point ($d = 1/8$) models by increasing the grid density, as shown in Figure 8. In these models, C, D, and E denote the three deepest actual physical measurement points for the corresponding layout. It should be noted that these points do not necessarily have identical spatial coordinates across the 5-point, 9-point, and 17-point models. As d decreases, the actual measurement region is compressed toward the deeper side of the structure: point E remains fixed at the deepest position, while points C and D are redefined according to the corresponding grid density and move closer to E, enabling the effect of a progressively deeper and more compressed measurement region to be evaluated. The points between the actual measurement region and the near-wall point A are treated as virtual points, denoted as B_1~B_5 for the 9-point model and B_1~B_{13} for the 17-point model.

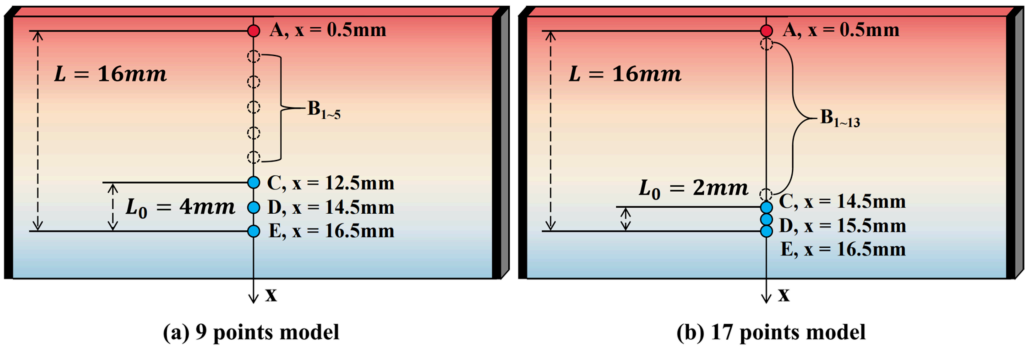


Figure 8. Schematics of extended heat conduction models under different measurement zone ratios d.

Taking the natural-convection boundary condition as a representative case, Figure 9 presents the reconstructed heated-surface temperatures for models with different measurement zone ratios d. The RRMSE values of the 9-point and 17-point models are 0.73% and 0.98%, respectively. Compared with the 5-point result in Figure 6b, the errors of the higher-order models are mainly concentrated near the step-heating transition points and at the initial cooling stage. This indicates that increasing the number of virtual recursive steps slightly weakens the ability of the method to capture abrupt temperature changes, resulting in minor overshoots or lags when the thermal signal varies rapidly.

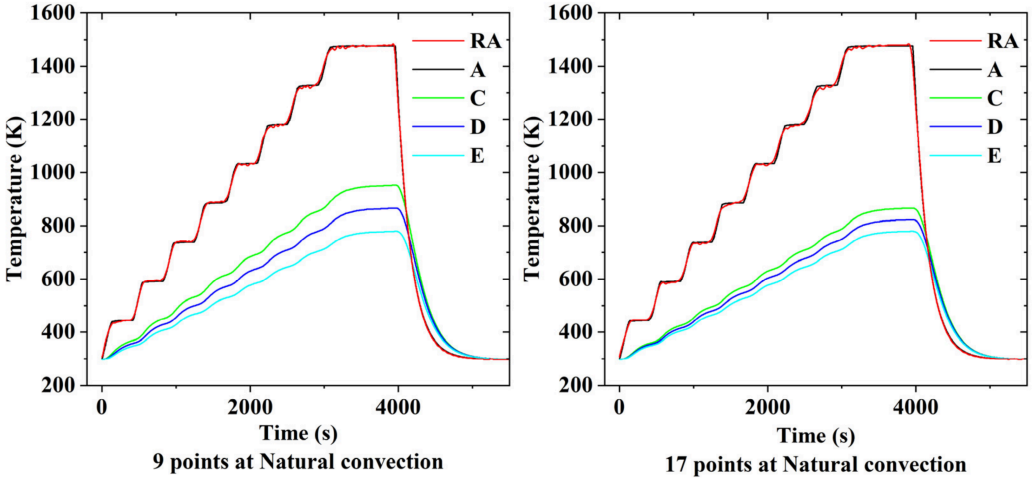


Figure 9. Reconstruction results of the heated surface temperature for extended models under natural convection conditions.

Figure 10 shows the variation in RRMSE as the measurement zone ratio d decreases from 2/3 to 1/8. The lowest RRMSE of 0.28% is obtained when the sensor array is relatively close to the heated surface (d = 2/3). As d decreases, the RRMSE generally increases, indicating that deeper and more compressed measurement regions lead to greater recursive extrapolation error. Nevertheless, even for the 17-point model with d = 1/8, the RRMSE remains 0.98%, demonstrating that the proposed method still maintains acceptable reconstruction accuracy in deeply embedded measurement scenarios.

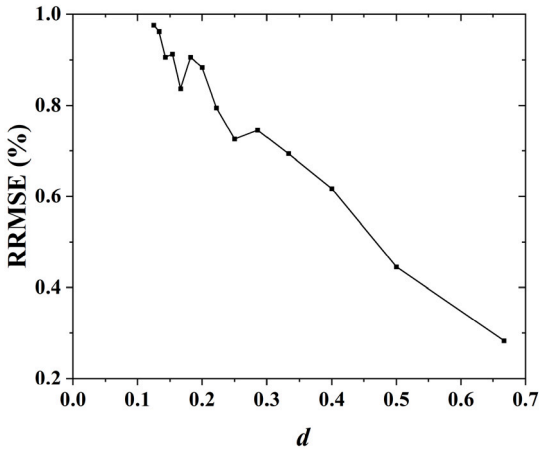


Figure 10. Variation trend of the RRMSE with respect to the measurement zone ratio d.

Figure 11 presents the RSD variations of each element in the identified parameter matrix **X**. As shown in Figure 11a, the RSD of τ increases monotonically as d decreases, with the maximum value approaching 3%. Since τ characterizes the thermal inertia and time-delay relationship between adjacent points, reducing the inter-point spacing weakens the distinguishability of temperature-response delays. This makes the ARX identification more sensitive to sampling noise and numerical truncation errors, thereby reducing parameter consistency.

In contrast, Figure 11b shows that the RSD of the geometric parameter ξ fluctuates slightly but remains at a very low level, below 0.35% for all tested d values. This is because ξ mainly represents the geometric thermal-resistance ratio between adjacent measurement zones, which is determined by the relative spatial arrangement of the points and is less affected by transient thermal-response delays. Therefore, compared with the dynamic

parameter τ, ξ exhibits stronger spatial stability. This comparison suggests that, as the number of virtual recursive steps increases, the error accumulation is more closely related to the identification uncertainty of τ than to that of ξ.

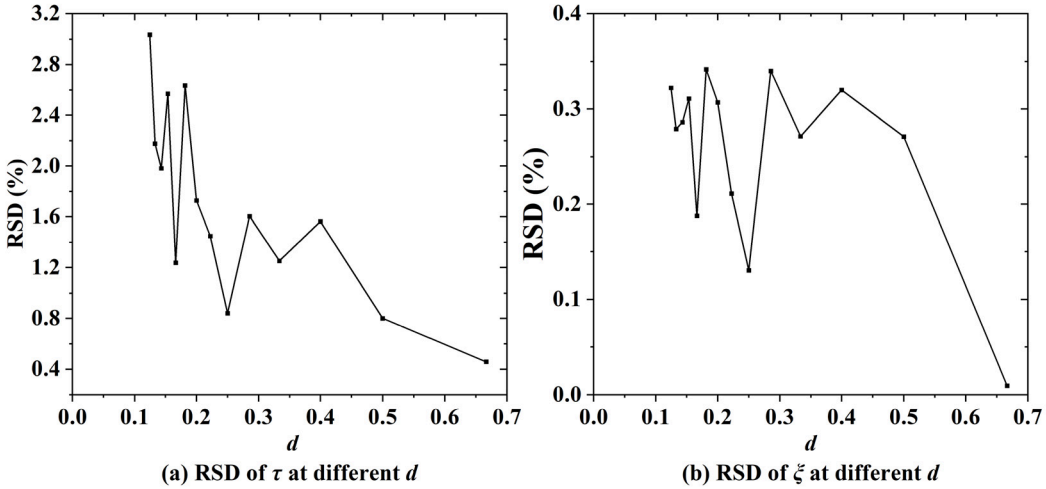


Figure 11. Evolution of the RSD for parameters τ and ξ under different measurement zone ratios d.

3.3. Sensitivity Analysis of Spatial Consistency Under Physical Sensor Position Deviations

Because Method 3 relies on the spatial consistency of the ARX parameter matrices identified from adjacent sub-regions, the uniformity of the physical sensor spacing is a key geometric constraint. This section focuses on the reconstruction error caused by the position deviations of physical sensors C and D within the actual C-D-E measurement region.

The baseline positions of the actual measurement points are x_C = 8.5 mm, x_D = 12.5 mm, and x_E = 16.5 mm, corresponding to a nominal spacing of 4 mm between adjacent physical sensors. To quantify the sensor-position deviation, the perturbation ratio ε_g is defined as the percentage deviation relative to this nominal 4 mm spacing. Two groups of perturbation tests were designed. In the first group, x_D and x_E were fixed, while the position of x_C was shifted according to the prescribed ε_g. In the second group, x_C and x_E were fixed, while the position of x_D was shifted according to the same perturbation ratio. The reconstruction accuracy was evaluated using the RRMSE of the reconstructed temperature at point A. The detailed coordinates of points C and D and the corresponding reconstruction errors are provided in Appendix B.

As shown in Figure 12, when the actual measurement point C or D deviates from the baseline uniform-spacing configuration, the reconstruction error of the surface temperature at point A increases significantly with the magnitude of the position deviation. This indicates that Method 3 is sensitive to the spacing uniformity of the physical sensors in the C-D-E measurement region. Taking RRMSE < 5% as the allowable error criterion, the permissible deviation range of point C is approximately $\varepsilon_g = \pm 6\%$ in the present case, whereas that of point D is approximately $\varepsilon_g = -5$~4%. This suggests that the position deviation of point D has a stronger influence on reconstruction accuracy than that of point C.

This difference is mainly associated with the geometric relationship within the C-D-E identification region. When point C is shifted, the deviation primarily changes the C-D spacing. In contrast, when point D is shifted, both the C-D and D-E spacings change simultaneously in opposite directions, which more directly modifies the geometric thermal-resistance ratio and local transfer characteristics of the C-D-E sub-region. Therefore, the deviation of point D more easily breaks the spatial consistency between the ARX parameter matrix identified from the C-D-E region and the upper recursive sub-regions, leading to a faster increase in reconstruction error.

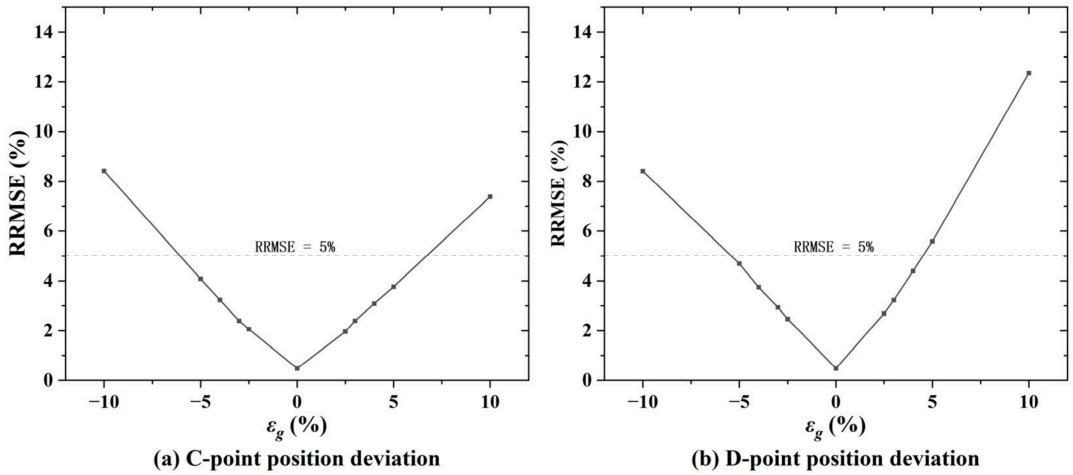


Figure 12. Reconstruction error under physical sensor position deviations: (**a**) RRMSE variation with C-point position deviation; and (**b**) RRMSE variation with D-point position deviation.

In addition, Figure 12 shows that the direction of the position deviation also affects the error growth. For point C, positive deviation produces a smaller accumulated error than negative deviation, whereas for point D, positive deviation produces a larger accumulated error than negative deviation. Considering both cases, the reconstruction error is relatively smaller when the deviation reduces the C-D spacing, while it is more easily amplified when the deviation increases the C-D spacing. This indicates that the C-D spacing is highly sensitive for deep-region parameter identification and virtual-point recursive extrapolation, further confirming that maintaining equal spacing among the actual measurement points C, D, and E is an important geometric condition for the validity of the spatial parameter consistency assumption.

3.4. Sensitivity Analysis of the Material Homogeneity Assumption Under Thermophysical Parameter Perturbations

In Method 3, the spatial consistency of the ARX parameter matrix depends not only on uniform physical sensor spacing but also on local material homogeneity. Here, material homogeneity does not require ρ, c, and k to remain globally constant over the entire TPS or throughout the whole heating process. Moderate and gradual variations in equivalent thermophysical properties are acceptable, but abrupt property changes between adjacent recursive sub-regions may weaken the equivalence among $\mathbf{X}_{ABC}$, $\mathbf{X}_{BCD}$, and $\mathbf{X}_{CDE}$, thereby reducing the reliability of virtual-point recursive extrapolation.

To quantify the sensitivity of Method 3 when the local material homogeneity assumption is not strictly satisfied, a controlled perturbation analysis of thermophysical parameters is conducted. While maintaining the architectures of the 5-point ($d = 1/2$), 9-point ($d = 1/4$), and 17-point ($d = 1/8$) models unchanged, linear variations of the thermophysical parameters with respect to temperature T or spatial coordinate x are artificially introduced, as formulated below:

$$P(var) = P_0 \cdot \left(1 + \eta \cdot \frac{var}{var_{\max}}\right) \tag{25}$$

where P represents the specific heat capacity c or thermal conductivity k; var denotes the independent variable, namely the instantaneous temperature T or the spatial coordinate x; η is the relative variation rate; and P_0 is the initial reference value. Since the density ρ is generally less sensitive to external thermal loading, and ρ and c enter Equation (4) through the volumetric heat-capacity term, the perturbation analysis is restricted to c and k.

The temperature-dependent cases $P(T)$ are used to evaluate the influence of thermophysical-property variations during heating, whereas the space-dependent cases $P(x)$ are treated as

controlled violations of the local material-homogeneity assumption. In the latter case, adjacent recursive sub-regions are assigned different equivalent thermophysical properties; therefore, a larger $|\eta|$ indicates a stronger departure from local homogeneity. The constant-parameter case ($\eta = 0$) serves as the reference condition. However, because the reconstruction error is also affected by thermal-response delay, sampling resolution, and recursive extrapolation error, the minimum RRMSE does not necessarily occur exactly at $\eta = 0$ for all datasets. The following subsections summarize the error characteristics for each perturbation group.

As shown in the left panel of Figure 13, when the specific heat capacity c varies linearly with temperature or space, the reconstruction error generally exhibits a U-shaped trend. For the 5-point and 9-point models, the minimum RRMSE values occur under the constant-parameter condition ($\eta = 0$), with errors of 0.45% and 0.73%, respectively. For the deeper 17-point model, however, the minimum error does not occur exactly at $\eta = 0$; the lowest RRMSE is obtained when c increases by 5% with temperature (RRMSE = 0.92%) or decreases by 10% along the spatial direction (RRMSE = 0.88%).

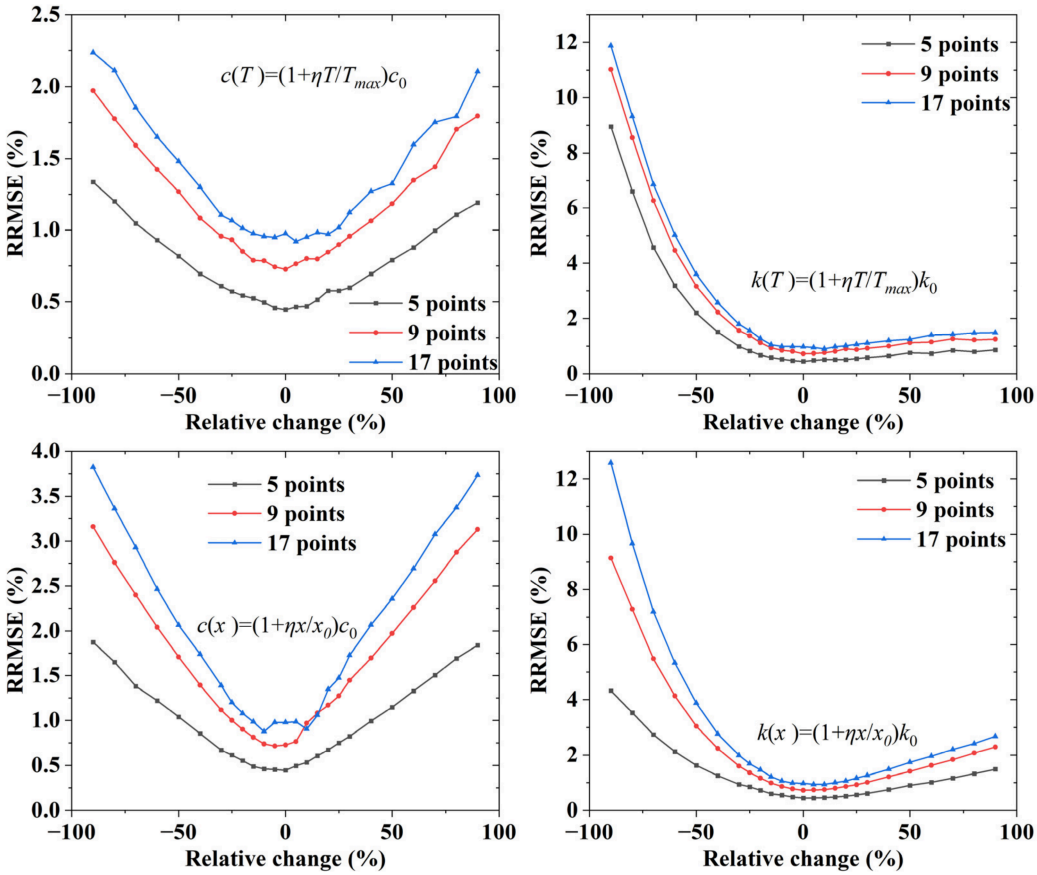


Figure 13. Variations of reconstruction error under linear perturbations of structural thermophysical parameters.

This slight non-monotonic behavior is mainly caused by the weak and indirect influence of specific heat capacity on the reconstruction process. Unlike thermal conductivity k, c primarily affects the heat storage and thermal response time through the volumetric heat-capacity term ρc, rather than directly modifying the conductive heat-flow path. Its effect can therefore be coupled with time delay, sampling resolution, and recursive extrapolation error. In the 17-point model, the larger number of virtual-recursion steps further amplifies small phase-lag and parameter-identification deviations, leading to local RRMSE fluctuations. Thus, the shifted minimum should be interpreted as a compensation be-

tween thermal-response delay and recursive extrapolation error, rather than as an accuracy improvement caused by material-parameter variation.

As shown in the right panel of Figure 13, the thermal conductivity k has a stronger influence on reconstruction accuracy than the specific heat capacity c, and the corresponding RRMSE curves show clear asymmetry. For the 5-point and 9-point models, the minimum errors occur at $\eta = 0$. For the 17-point model, the minimum RRMSE values for the temperature- and space-dependent cases both occur at $\eta = 10\%$, with errors of 0.90% and 0.93%, respectively. When k increases ($\eta > 0$), the RRMSE remains relatively stable because higher thermal conductivity enhances the transmission of thermal signals from the heated surface to the deep sensors. In contrast, when k decreases ($\eta < 0$), the thermal signal is more strongly attenuated and the reconstruction error increases rapidly. For example, when the variation rate of $k(T)$ reaches -90%, the RRMSE increases to 8.95%.

Overall, the perturbation results show that the reconstruction error is more sensitive to variations in thermal conductivity k than to variations in specific heat capacity c. Taking the 5-point model with temperature-dependent parameters as an example, when $\eta = \pm 90\%$, the maximum RRMSE values caused by c variations are 1.19% and 1.34%, respectively, whereas those caused by k variations reach 1.49% and 8.95%. For both c and k, negative variations ($\eta < 0$) generally lead to larger errors than positive variations ($\eta > 0$), because reduced thermophysical properties intensify the attenuation and delay of thermal signals received by deep sensors. Nevertheless, within the range of $\eta \in [-50\%, 50\%]$, the RRMSE remains approximately below 2% even for the deeply embedded 17-point model, indicating that the proposed method can tolerate moderate temperature- and space-dependent variations in equivalent thermophysical properties.

These results show that the material-homogeneity requirement in Method 3 should be interpreted as a local slow-variation condition rather than an absolute constant-property assumption. The method can tolerate moderate and gradual variations in equivalent thermophysical properties, but sharp decreases in k or strong spatial non-homogeneity may attenuate deep thermal signals, weaken the spatial consistency of the ARX parameter matrices, and rapidly increase the reconstruction error.

3.5. Equivalent TPS Thermal-Degradation Simulation Using Realistic LI-900 Thermal Conductivity Variations

During long-term service, the effective thermal-insulation performance of TPS may deviate from the nominal state because of service-induced damage, interface degradation, surface/coating damage, environmental exposure, aging, and other system-level effects. In reduced-order thermal reconstruction models, these comprehensive effects can be approximately represented by variations in effective thermal conductivity. Therefore, this section constructs equivalent thermal-degradation scenarios using realistic thermal-conductivity data of NASA LI-900 insulation. LI-900 is selected because it is one of the most representative low-density ceramic insulation materials used in reusable TPS; its thermophysical properties have been extensively characterized by NASA, providing a reliable and well-established engineering dataset for constructing representative conductivity conditions. Five representative thermal-conductivity curves (TC1–TC5) are selected to evaluate the proposed method under different effective thermal-response conditions, as shown in Figure 14a. TC1–TC5 correspond to the thermal-conductivity data of LI-900 under different ambient pressures: TC1 represents the low-pressure condition of 10.133 Pa, TC5 corresponds to standard atmospheric pressure of approximately 101 kPa, and TC2–TC4 correspond to pressure levels increasing successively by one order of magnitude. Thus, TC1 and TC5 represent the lowest and highest effective thermal-conductivity conditions considered in this study, respectively.

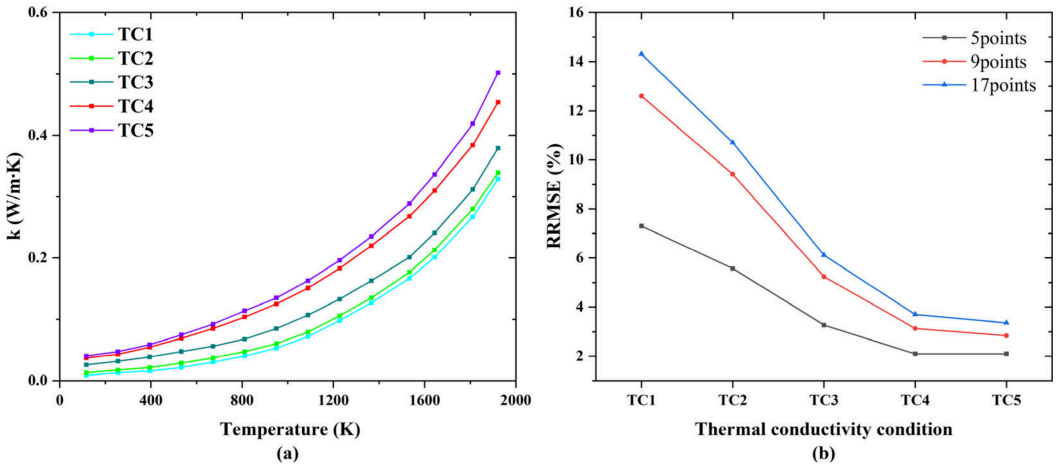


Figure 14. Equivalent degradation simulation based on realistic LI-900 thermal conductivity variations: (**a**) thermal conductivity curves of LI-900 under different ambient pressure conditions, from TC1 to TC5; and (**b**) global RRMSE statistics of the 5-point, 9-point, and 17-point models under the corresponding TC1–TC5 thermal conductivity conditions.

The RRMSE statistics of the 5-point, 9-point, and 17-point models under the TC1–TC5 conditions are shown in Figure 14b. As the effective thermal conductivity increases from TC1 to TC5, the reconstruction error generally decreases. For the TC5 condition, the RRMSE decreases to 2.10% for the 5-point model and remains 3.36% even for the deeply embedded 17-point model. This indicates that higher thermal conductivity enhances the transmission of thermal signals to the deep measurement region, enabling the embedded sensors to capture clearer temperature responses. In contrast, under the TC1 condition with extremely low thermal conductivity, the reconstruction error is relatively larger, reaching approximately 7.30% for the 5-point model. This is mainly because strong thermal insulation leads to severe attenuation and delay of the deep thermal signals, making surface-temperature reconstruction from embedded measurements more difficult.

These results suggest that the applicability of the proposed method depends on the strength of the thermal information received by the embedded sensors. Under the low-conductivity TC1 and TC2 conditions, the deep thermal signals are strongly attenuated and the reconstruction accuracy of the 9-point and 17-point models is limited; only the 5-point model maintains relatively acceptable performance because of its fewer recursive steps and less compressed measurement region. As the effective thermal conductivity increases from TC3 to TC5, the internal thermal responses become clearer and the reconstruction accuracy of all three models improves. Therefore, the proposed method can provide reliable surface-temperature information for long-term TPS thermal-state monitoring, even when the local effective thermal response deviates from its nominal condition, provided that sufficient internal temperature-difference information is available.

4. Experimental Verification

4.1. Experimental Method

To verify the effectiveness of the iterative reconstruction algorithm in a realistic thermal environment, a single-sided heating surface temperature reconstruction experimental platform was constructed, as illustrated in Figure 15. The system is primarily composed of a heating stage, a base plate, insulation cotton, a multi-channel temperature data acquisition system, and a data processing computer. The experiment employed a laboratory-fabricated ceramic insulation tile as the test object, which was machined into a cubic specimen with dimensions of 40 mm × 40 mm × 40 mm. To construct a quasi one-dimensional heat

conduction environment, the lateral sides of the specimen were wrapped with multi-layer insulation cotton to simulate adiabatic boundaries. Because direct placement of a thermocouple on the contact surface would disturb the uniform contact between the specimen and the heating stage, thermocouple A was embedded close to the heated surface rather than mounted directly on it. Accordingly, the measured temperature at point A was used as the near-surface reference temperature for evaluating the reconstruction accuracy, while the base plate was utilized to ensure uniform heating across the heated surface.

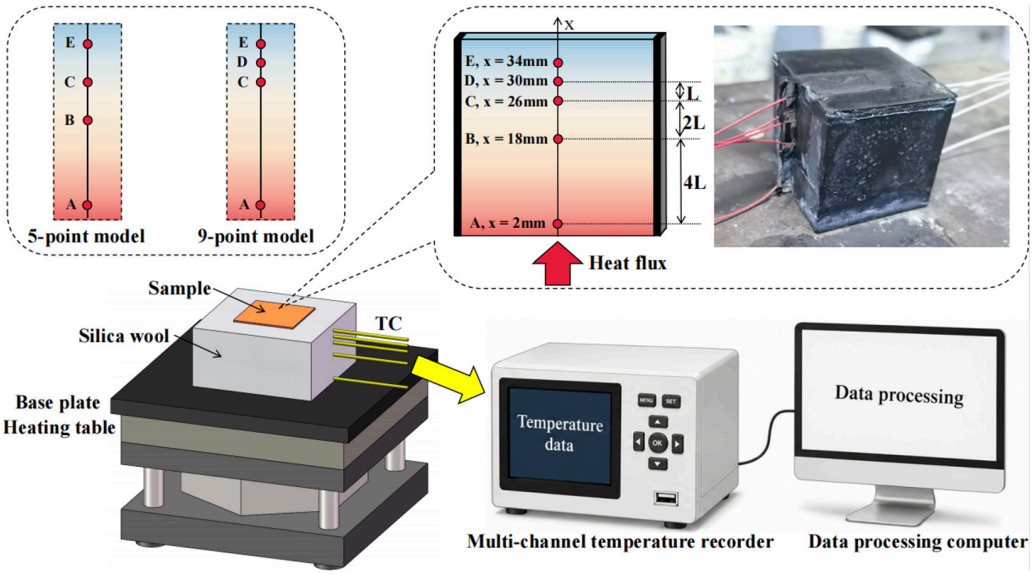


Figure 15. Schematic diagram of the surface temperature reconstruction experimental platform and the sensor layout within the specimen.

The core of this experiment lies in the non-uniform spatial layout strategy of the internal thermocouples. As depicted in Figure 15, five measurement points (A, B, C, D, and E) were embedded at varying depths along the central axis perpendicular to the heated surface. Based on a minimum unit spacing of L = 4 mm, the coordinates of each measurement point relative to the heated surface (x = 0) are configured as follows: x_A = 2 mm, x_B = 18 mm, x_C = 26 mm, x_D = 30 mm, and x_E = 34 mm. This specific non-uniform layout allows for the simultaneous validation of two reconstruction models with different measurement zone ratios d within a single experimental run by selecting different combinations of sensors. Specifically, thermocouples A, B, C, and E constitute the validation set for the 5-point model ($d = 4L/8L = 1/2$), while thermocouples A, C, D, and E constitute the validation set for the 9-point model ($d = 2L/8L = 1/4$).

During the experiment, the heating stage was configured with a predefined heating curve to apply single-sided heating to the bottom surface (x = 0) of the specimen. All thermocouple signals were synchronously acquired by a multi-channel data recorder and transmitted to the host computer. In the subsequent data processing, the temperature measurements from points B, C, D, and E were used as inputs to the reconstruction algorithm. The reconstructed temperature at point A, denoted as RA, was then compared with the measured temperature from thermocouple A to quantitatively evaluate the reconstruction accuracy.

4.2. Experimental Results and Analysis

Five single-sided heating experiments were conducted to evaluate the adaptability of the proposed method under different transient thermal histories. These include one main validation experiment and four supplementary experiments with different heating rates, dwell durations, cooling paths, and numbers of heating stages. The de-

tailed heating and cooling histories, including the duration of each stage, are summarized in Appendix C, Table A3.

Figure 16 illustrates the comparison between the inverted temperature (RA) and the measured temperature for both the 5-point model (d = 1/2) and the 9-point model (d = 1/4), along with the time-domain evolution of the instantaneous relative error. The results demonstrate that both models successfully reconstructed the dynamic temperature trajectory of the heated surface, accurately capturing even the complex inflection points of the heating steps. The RRMSEs for the 5-point and 9-point models are 1.74% and 4.27%, respectively, both exhibiting excellent accuracy.

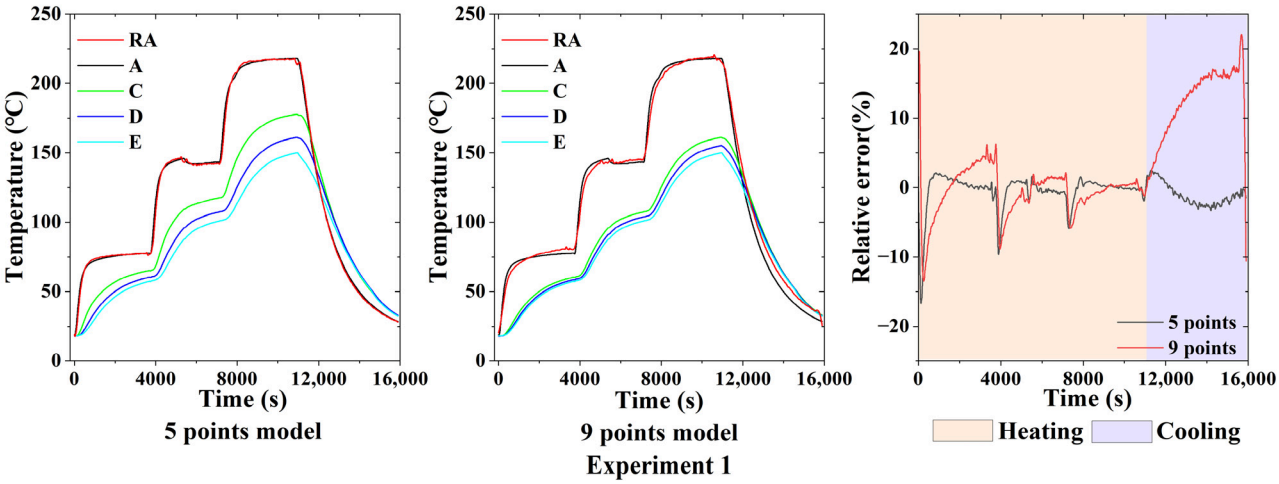


Figure 16. Reconstruction results and error analysis of the heated surface temperature in Experiment 1.

As shown in the error curves, the error peaks during the heating phase mainly occur at the initial moments of abrupt temperature changes and then rapidly decrease as the temperature response stabilizes. This indicates a slight response lag of the reconstruction method when tracking rapid thermal transients. During the cooling phase, the 5-point and 9-point models show different error characteristics. The error of the 5-point model fluctuates at around zero, whereas the 9-point model exhibits a more evident drift. This is mainly because the 9-point model uses deeper measurement points and involves more virtual recursive steps, making it more sensitive to the weakened temperature-difference information during cooling. A more detailed discussion of the influence of the low internal temperature-difference signal-to-noise ratio (SNR) on the reconstruction error is provided in Section 5.

To further verify the adaptability of the proposed method under different thermal loading conditions, four additional experiments were conducted, as summarized in Figure 17. The results show that the method maintains stable tracking performance under different transient thermal histories. The RRMSE of the 5-point model ranges from 1.36% to 2.33%, whereas that of the 9-point model ranges from 2.72% to 3.87%. The 5-point model consistently achieves higher reconstruction accuracy because it involves fewer recursive steps and a less compressed measurement region. Although the 9-point model introduces a deeper measurement layout (d = 1/4) and shows localized deviations during cooling, it still maintains relatively low errors during the heating stage, with instantaneous relative errors generally below 5%. Overall, the five experimental cases demonstrate the validity and adaptability of the proposed reconstruction method under different transient heating conditions.

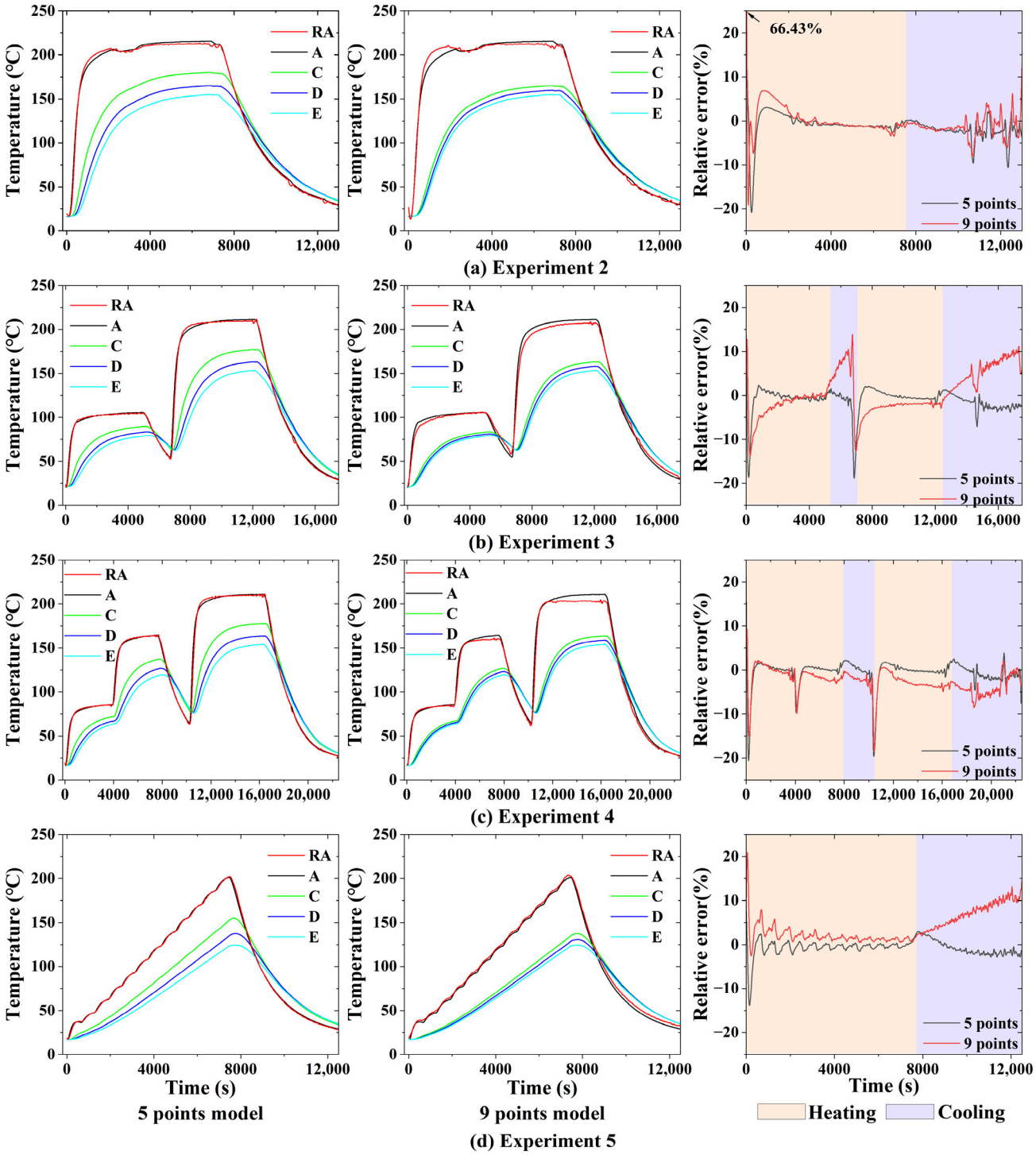


Figure 17. Reconstruction results and error analysis under different transient heating conditions.

5. Discussion

5.1. Internal Temperature-Difference SNR Requirement for Stable ARX Identification

To further discuss the temperature-gradient constraint for stable ARX identification, Experiment 1 was selected as a representative case because it contains the main heating–dwelling–cooling process and includes both the 5-point and 9-point reconstruction results. For each model, points C, D, and E refer to the three actual physical sensors used for ARX

parameter identification in the corresponding layout. The internal temperature-difference signal-to-noise ratio is defined as:

$$S_T(t) = \frac{\Delta T_{\min}(t)}{\sigma_T} \tag{26}$$

where

$$\Delta T_{\min}(t) = \min(|T_C(t) - T_D(t)|, |T_D(t) - T_E(t)|) \tag{27}$$

and σ_T denotes the measurement uncertainty of the thermocouple system. A larger S_T indicates stronger effective differential information between adjacent embedded sensors, whereas a smaller S_T indicates a low-gradient and low-SNR condition.

Figure 18 shows the S_T-based error statistics of the 5-point and 9-point models in Experiment 1. For the 5-point model, the bin-wise RRMSE is 3.73% when $S_T < 2$ but decreases to 0.62% when S_T increases to $6 \leq S_T < 8$. This result indicates that a higher adjacent sensor temperature-difference SNR provides more effective differential information for ARX parameter identification and virtual-point extrapolation. The corresponding S_T-based statistics for the other four experiments are provided in Appendix D.

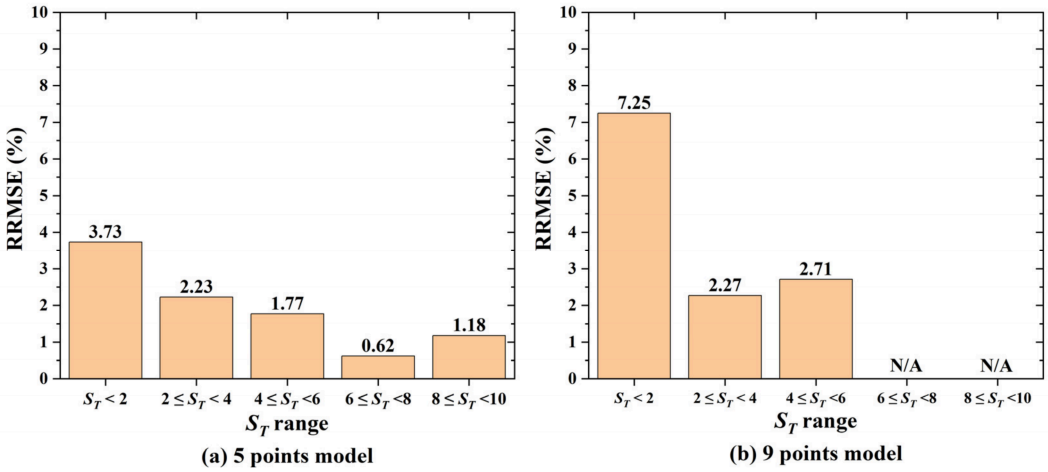


Figure 18. RRMSE statistics under different internal temperature-difference SNR (S_T) ranges in Experiment 1: (**a**) five-point model; and (**b**) nine-point model.

In contrast, the S_T distribution of the 9-point model shifts toward the lower-SNR range, with no samples observed for $S_T \geq 6$. This is mainly because the C-D-E sensor triplet used in the 9-point model is located deeper and has smaller inter-point spacing, which reduces the adjacent temperature differences. In the $S_T < 2$ range, the RRMSE reaches 7.25% and the maximum instantaneous relative error reaches 22.02%, confirming that insufficient adjacent sensor temperature-difference information can reduce the stability of ARX identification.

The RRMSE values do not vary strictly monotonically across all S_T ranges because the sample numbers and corresponding transient thermal stages differ among bins. For example, in the 9-point model, the $4 \leq S_T < 6$ range contains only 288 samples, making this statistic more susceptible to local dynamic errors.

Overall, the results show that deeper and more compressed measurement layouts reduce the internal temperature-difference SNR and make the reconstruction more sensitive to low-gradient conditions. Therefore, S_T can be used as an indicator of whether a deeply embedded sensor layout provides sufficient effective temperature-difference information for stable ARX identification.

5.2. Error Propagation in Multi-Step Virtual-Point Recursion

In Method 3, the near-surface temperature is reconstructed through layer-by-layer virtual-point recursion. Therefore, the final reconstruction error is not only related to the ARX parameter-identification accuracy in the deepest physical measurement region, but also to the propagation and accumulation of errors during recursive extrapolation. To clarify the relationship between recursion depth and error accumulation, an upper-bound error-transfer model is introduced here. The detailed derivation is provided in Appendix E.

For an m-step virtual-point recursion process, the accumulated reconstruction error can be bounded as:

$$\|e_0\|_\infty \le \left(\prod_{i=1}^{m} G_i\right)\|e_m\|_\infty + \sum_{j=1}^{m}\left(\prod_{i=1}^{j-1} G_i\right)\|\varepsilon_j\|_\infty \tag{28}$$

where e_0 is the final near-surface reconstruction error, e_m is the error propagated from the deepest physical measurement region, m is the number of virtual recursive steps, G_i is the effective amplification factor of the i-th recursive step, and ε_i denotes the additional error introduced at that step. The term ε_i includes ARX parameter-identification deviation, measurement noise, spatial-consistency deviation between adjacent sub-regions, finite-difference truncation error, and numerical perturbations under low-gradient conditions:

$$\|e_0\|_\infty \le G^m\|e_m\|_\infty + \varepsilon\frac{G^m-1}{G-1}, G \ne 1 \tag{29}$$

When $G \approx 1$, the accumulated error becomes approximately:

$$\|e_0\|_\infty \le \|e_m\|_\infty + m\varepsilon \tag{30}$$

Equations (29) and (30) provide simplified upper-bound forms of Equation (28). Under the assumptions $G_i \approx G$ and $\|\varepsilon_i\|_\infty \le \varepsilon$, the accumulated error is mainly governed by the recursion depth m, the representative single-step amplification factor G, and the upper bound ε of the additional error. When G is close to unity, the error accumulates approximately linearly with m. When $G > 1$, the error may be amplified more rapidly during recursive extrapolation. This explains why the reconstruction error tends to increase when the measurement zone ratio d decreases, and more virtual points are introduced between the physical measurement region and the target point. In practical sensor-layout design, reducing unnecessary recursion steps and ensuring high-quality deep measurement signals are, therefore, beneficial for improving reconstruction stability.

5.3. Regularization Strategy Under Low-Gradient and Low-SNR Conditions

In the proposed method, the ARX parameter matrix is identified using ordinary least squares. Under sufficient temperature-gradient conditions, the embedded measurement points provide effective differential information and the regression matrix can be identified stably. However, when the temperature responses of adjacent embedded sensors become close under low-gradient and low-S_T conditions, the effective differential information in the regression matrix is weakened. As a result, the least squares solution becomes more sensitive to measurement noise and numerical perturbations.

To extend the applicability of ARX parameter identification to low-gradient and low-S_T conditions, a Tikhonov-regularized least squares formulation is introduced as:

$$\mathbf{X}_\lambda = (\mathbf{B}^{\mathrm{T}}\mathbf{B} + \lambda\mathbf{I})^{-1}\mathbf{B}^{\mathrm{T}}\mathbf{A} \tag{31}$$

where $\mathbf{B}$ is the ARX regression matrix, $\mathbf{A}$ is the observation vector, $\mathbf{I}$ is the identity matrix, and λ is the regularization parameter. Compared with ordinary least squares solution, the additional term $\lambda\mathbf{I}$ improves the conditioning of $\mathbf{B}^{\mathrm{T}}\mathbf{B}$ and suppresses excessive fluctuations in the identified parameters when the effective temperature-difference information is insufficient.

In this study, the regularization parameter is scaled according to the magnitude of the regression matrix:

$$\lambda = \lambda_0 \frac{\mathrm{tr}(\mathbf{B}^{\mathrm{T}}\mathbf{B})}{n} \tag{32}$$

where λ_0 is a dimensionless scanning parameter, $\mathrm{tr}(\mathbf{B}^{\mathrm{T}}\mathbf{B})$ is the trace of $\mathbf{B}^{\mathrm{T}}\mathbf{B}$, and n is the number of identified parameters. This scaling makes the regularization strength adaptive to the magnitude of the regression matrix. The value of λ_0 is not selected by minimizing the condition number alone. Instead, it is determined by jointly considering the full-domain RRMSE, the RRMSE in the low-S_T range, and the maximum instantaneous relative error in the low-S_T range. This is because an excessively large regularization parameter may reduce the condition number but also introduce bias into the identified ARX parameters, thereby degrading the reconstruction accuracy.

To evaluate the regularized solution under more challenging low-S_T conditions, the five 9-point experimental cases were tested. The detailed comparison between ordinary least squares and the selected Tikhonov-regularized results is provided in Appendix F. Here, Experiment 3 is selected as a representative case. For ordinary least squares, the condition number of $\mathbf{B}^{\mathrm{T}}\mathbf{B}$ is 7.02×10^7, the full-domain RRMSE is 3.87%, and the RRMSE and maximum instantaneous relative error in the $S_T < 2$ range are 5.75% and 84.12%, respectively. After applying Tikhonov regularization with $\lambda_0 = 3.00 \times 10^{-9}$, these values decrease to 6.56×10^7, 3.43%, 5.49%, and 77.21%, respectively. This result indicates that moderate regularization can reduce the sensitivity of ARX parameter identification to low-gradient and low-S_T conditions and suppress local error peaks.

It should also be noted that regularization does not monotonically improve reconstruction accuracy. As summarized in Appendix F, its effect varies among the five experimental cases. In Experiment 4, no regularization parameter satisfying the selection constraints is found; although increasing λ_0 reduces the condition number, both the full-domain RRMSE and the low-S_T errors increase. In Experiments 1 and 2, regularization slightly suppresses the maximum instantaneous error in the $S_T < 2$ range, but this is accompanied by a small increase in full-domain RRMSE. In Experiment 5, the selected parameter reduces the $S_T < 2$ RRMSE and maximum instantaneous error, but also slightly increases the full-domain RRMSE. These results indicate that regularization should be applied adaptively rather than used as a universal replacement for ordinary least squares.

It should be clarified that the RRMSE-based selection of λ_0 in this study is used for offline validation of the regularization strategy. The reference temperature at point A is used only to compare different regularization strengths and evaluate their influence on reconstruction accuracy. In practical online applications, λ_0 should be predetermined through calibration experiments, historical datasets, numerical simulations, or cross-validation according to the thermal history and data characteristics of the target structure. Once λ_0 is selected, the online reconstruction process requires only the embedded sensor data and does not require prior knowledge of the surface temperature or thermophysical properties. Therefore, Tikhonov regularization should be regarded as an optional stabilization strategy for low-gradient and low-S_T conditions, rather than as a fixed component applied to all cases. Its use should jointly consider the matrix conditioning, the low-S_T reconstruction error, the suppression of local error peaks, and the allowable loss of full-domain accuracy.

5.4. Quantitative Design Method for Embedded Sensor Layout

Although the previous sections evaluate several fixed sensor layouts and measurement-zone ratios, practical engineering applications require a systematic procedure for selecting the physical sensor triplet, sensor spacing, and allowable embedding depth. For the ARX formulation used in this study, three physical measurement points are required to construct one local identification sub-region. Therefore, the layout design focuses on whether the selected sensor triplet can provide sufficient effective temperature-difference information while keeping the measurement region sufficiently far from the heated surface. Based on the preceding analyses of measurement-zone ratio, sensor-position deviation, internal temperature-difference SNR, error propagation, and regularization, this section proposes a sensor-layout design method constrained by the target reconstruction accuracy and effective temperature-difference information.

First, the target reconstruction accuracy should be specified according to the engineering requirement such as an allowable RRMSE E_{target}. The measurement uncertainty of the embedded sensor, denoted as σ_T, should also be determined from the sensor calibration or manufacturer's specifications. For a candidate layout, three adjacent embedded sensors, T_1, T_2, and T_3, are selected to form the local ARX identification sub-region. The internal temperature-difference SNR S_T can then be evaluated using the same definition as in Equation (26), where $\Delta T_{min}(t) = min(|T_1(t) - T_2(t)|, |T_2(t) - T_3(t)|)$. A reliable layout should avoid a long-term concentration of samples in the low-S_T range. Based on the experimental analysis in Section 5.1, $S_T < 2$ can be regarded as a low-SNR warning region under the present experimental conditions. Therefore, when selecting the physical sensor triplet and its embedding depth, the proportion of low-S_T samples should be controlled within an acceptable range to ensure sufficient differential temperature information for ARX identification.

Second, the physical sensor spacing should satisfy a local geometric-uniformity constraint. The sensor-position perturbation analysis shows that deviations from uniform spacing can increase the reconstruction error. For the tested 4 mm baseline spacing, maintaining RRMSE < 5% allows for position deviations of approximately ±6% for point C and −5% to +4% for point D. Therefore, under similar structural and thermal conditions, the relative spacing deviation between adjacent physical sensors is recommended to be controlled to within approximately 5%.

Third, for the ARX formulation used in this study, three physical measurement points are required to construct one local identification sub-region. Thus, sensor-layout design should focus on selecting an appropriate physical sensor triplet and embedding depth rather than increasing the number of input points in a single ARX identification. If the selected measurement region is too deep, more virtual recursive steps are required, and the accumulated error increases according to the error-transfer relationship discussed in Section 5.2. Therefore, the selected sensor triplet should be placed as deep as necessary for sensor survivability, but not so deep that excessive virtual recursion is introduced.

Finally, the allowable maximum embedding depth should be determined by jointly considering the target reconstruction accuracy, the internal temperature-difference SNR, and the required virtual-recursion depth. For a candidate sensor triplet with the deepest point located at $x_{\max}$, the layout should satisfy:

$$\text{RRMSE}(x_{\max}) \leq E_{\text{target}} \tag{33}$$

and the proportion of low-S_T samples during the main thermal-response stage should be limited:

$$p_{\mathrm{low}}(x_{\max}) = \frac{N(S_T(t;\, x_{\max}) < S_{\min})}{N_{\mathrm{total}}} \le p_{\mathrm{allow}} \tag{34}$$

where E_{target} is the allowable reconstruction error, $S_{\min}$ is the minimum acceptable temperature-difference SNR threshold, $N()$ denotes the number of samples satisfying the condition, N_{total} is the total number of samples in the main thermal-response stage, and p_{allow} is the allowable proportion of low-S_T samples. Here, RRMSE($x_{\max}$) is evaluated during the design or calibration stage using numerical simulations, calibration experiments, or historical reference data.

If these constraints are not satisfied, the selected sensor triplet should be moved closer to the target surface, the sensor spacing should be adjusted to increase the measurable temperature difference, or the virtual-recursion depth should be reduced. When low-S_T intervals cannot be avoided, the regularized ARX solution discussed in Section 5.3 can be used as an optional stabilization strategy, but it should not replace the primary layout optimization.

6. Conclusions

This study proposes an ARX-based surface temperature reconstruction method using deep-embedded sensors for thermal protection structures. By identifying a local equivalent dynamic mapping among internal temperature responses and introducing virtual-point recursive extrapolation, the method reconstructs the near-surface temperature without requiring explicit thermophysical-property functions or boundary-condition information.

Numerical simulations show that the method maintains high accuracy under adiabatic, natural-convection, and forced-convection boundary conditions, with the global RRMSE remaining within 1.09%. When the measurement zone is further compressed toward the deeper region, the reconstruction error increases because more virtual recursive steps are introduced; nevertheless, the RRMSE remains 0.98% even for the 17-point model with $d = 1/8$. Sensitivity analyses further indicate that the method can tolerate moderate and gradual variations in equivalent thermophysical properties, although sharp decreases in thermal conductivity or strong spatial non-homogeneity may weaken the deep thermal signals and increase the reconstruction error.

Single-sided heating experiments further verify the practical applicability of the proposed method. In the main validation experiment, the RRMSE values of the 5-point and 9-point models are 1.74% and 4.27%, respectively. In four additional experiments with different transient thermal histories, the RRMSE ranges from 1.36% to 2.33% for the 5-point model and from 2.72% to 3.87% for the 9-point model. The discussion based on internal temperature-difference SNR, error propagation, regularization, and sensor-layout design clarifies the applicable conditions of the method: the selected physical sensor triplet should provide sufficient effective temperature-difference information, and excessive virtual-recursion depth should be avoided. Overall, the proposed method provides a feasible low-cost and long-life solution for online TPS surface temperature monitoring using deeply embedded sensors.

Future research will be dedicated to extending this one-dimensional framework to complex two-dimensional and three-dimensional structures, utilizing distributed sensor networks to achieve global real-time reconstruction of the surface temperature field over large-area TPS of flight vehicles.

Author Contributions: Conceptualization, P.N.; methodology, B.S. and X.W.; software, B.S.; validation, B.S. and X.W.; formal analysis, B.S.; investigation, B.S.; resources, H.Y.; data curation, B.S.; writing—original draft preparation, B.S.; writing—review and editing, H.Y.; visualization, B.S.; supervision, P.N. and H.Y.; project administration, G.X. and H.Y.; funding acquisition, G.X. All authors have read and agreed to the published version of the manuscript.

Funding: This research was funded by the National Natural Science Foundation of China (12304346), Key Research and Development Projects of Shaanxi Province (2025CY-YBXM-073), Donghai Laboratory (2024SSYS0091), and the Open Fund of Beijing Key Laboratory of Advanced Optical Remote Sensing Technology (AORS202408).

Data Availability Statement: Dataset available on request from the authors.

Conflicts of Interest: The authors declare no conflicts of interest.

Abbreviations

The following abbreviations are used in this manuscript:

TPS	Thermal Protection Structures
ARX	AutoRegressive with eXogenous input
RRMSE	Relative Root Mean Square Error
SNR	Signal-to-Noise Ratio
PINN	Physics-Informed Neural Networks

Appendix A. Through-Thickness Temperature-Gradient Evolution During the Simulated Cooling Stage

To further explain the higher relative error observed under the adiabatic condition after 4000 s, the through-thickness temperature distributions during the cooling stage are compared under the three cold-side boundary conditions, as shown in Figure A1. Although the near-surface temperature histories under different boundary conditions show similar cooling trends, the internal temperature fields are not identical.

Under the adiabatic boundary condition, heat cannot dissipate through the rear surface. During cooling, the prescribed near-surface temperature decreases rapidly, whereas the deeper region retains a large amount of stored heat because of the insulated rear boundary. Therefore, the internal heat is mainly released toward the cooled heated surface. This produces a temporary mismatch between rapid near-surface cooling and delayed internal thermal response, causing a lagging error in the virtual-point extrapolation.

Meanwhile, the adiabatic condition tends to homogenize the internal temperature field during the late cooling stage. As the temperature differences between adjacent measurement points decrease, the effective differential information used for ARX parameter identification becomes weaker. This makes the recursive extrapolation more sensitive to small numerical or measurement perturbations and may introduce accumulated deviations.

As cooling continues, the surface temperature variation rate decreases and the internal temperature field is gradually readjusted through heat release toward the cooled surface. Consequently, the dynamic lagging effect weakens, and the instantaneous relative error decreases after the initial peak. In contrast, natural and forced convection at the rear surface provide an additional heat-dissipation path, helping to maintain a more pronounced through-thickness temperature gradient and more stable ARX identification during the cooling stage.

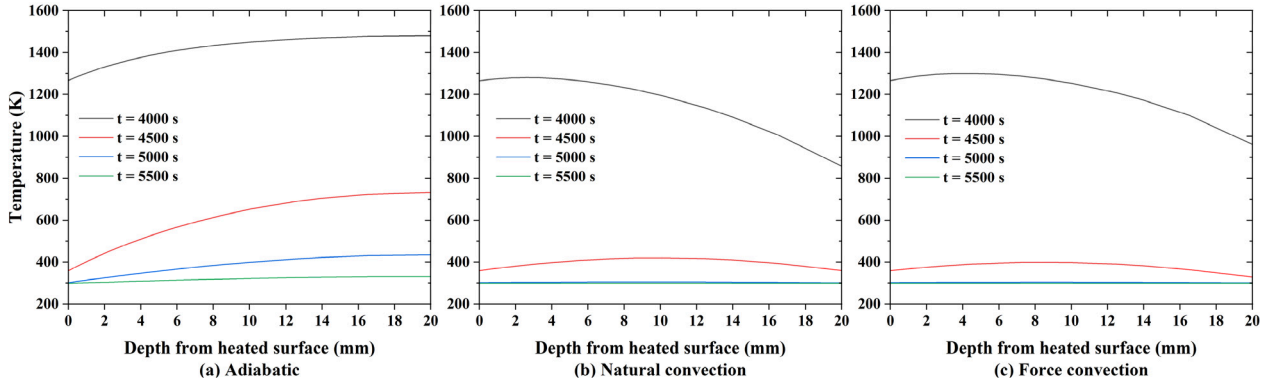


Figure A1. Through-thickness temperature-gradient evolution during the simulated cooling stage under different cold-side boundary conditions: (**a**) adiabatic boundary; (**b**) natural-convection boundary; and (**c**) forced-convection boundary.

Appendix B. Detailed Sensor Arrangements and Reconstruction Errors for C- and D-Point Position Deviations

Table A1. Sensitivity of reconstruction accuracy to C-point position deviation.

ε_g	x_C/mm	x_D/mm	x_E/mm	RRMSE/%
−10%	8.1	12.5	16.5	8.42
−7%	8.22	12.5	16.5	5.77
−6%	8.26	12.5	16.5	4.94
−5%	8.3	12.5	16.5	4.08
−4%	8.34	12.5	16.5	3.24
−3%	8.38	12.5	16.5	2.40
−2.5%	8.4	12.5	16.5	2.06
0	8.5	12.5	16.5	0.48
2.5%	8.6	12.5	16.5	1.96
3%	8.62	12.5	16.5	2.40
4%	8.66	12.5	16.5	3.09
5%	8.7	12.5	16.5	3.77
6%	8.74	12.5	16.5	4.58
7%	8.78	12.5	16.5	5.30
10%	8.9	12.5	16.5	7.38

Table A2. Sensitivity of reconstruction accuracy to D-point position deviation.

ε_g	x_C/mm	x_D/mm	x_E/mm	RRMSE/%
−10%	8.5	12.1	16.5	8.41
−5%	8.5	12.3	16.5	4.69
−4%	8.5	12.34	16.5	3.75
−3%	8.5	12.38	16.5	2.94
−2.5%	8.5	12.4	16.5	2.47
0	8.5	12.5	16.5	0.48
2.5%	8.5	12.6	16.5	2.69
3%	8.5	12.62	16.5	3.23
4%	8.5	12.66	16.5	4.39
5%	8.5	12.7	16.5	5.59
10%	8.5	12.9	16.5	12.35

Appendix C. Detailed Temperature Histories of the Five Single-Sided Heating Experiments

Table A3. Temperature programs and durations of the five experimental cases.

Case	Figure	Stage Duration	Total Duration
Experiment 1	Figure 16	Heating: 0–720 s; Holding: 720–3520 s; Heating: 3520–4240 s; Holding: 4240–7040 s; Heating: 7040–7760 s; Holding: 7760–10,560 s; Cooling: 10,560–16,000 s	16,000 s
Experiment 2	Figure 17a	Heating: 0–1500 s; Holding: 1500–7300 s; Cooling: 7300–13,000 s	13,000 s
Experiment 3	Figure 17b	Heating: 0–600 s; Holding: 600–5000 s; Cooling: 5000–6600 s; Heating: 6600–7500 s; Holding: 7500–12,000 s; Cooling: 12,000–17,400 s;	17,400 s
Experiment 4	Figure 17c	Heating: 0–900 s; Holding: 900–3600 s; Heating: 3600–4800 s; Holding: 4800–7500 s; Cooling: 7500–10,300 s; Heating: 10,300–11,000 s; Holding: 11,000–16,400 s; Cooling: 16,400–22,400 s;	22,400 s
Experiment 5	Figure 17d	Heating: 0–240 s; Holding: 240–620 s; Repeated a total of 10 times Heating: 6820–7060 s; Holding: 7060–7440 s; Cooling: 7440–12,500 s;	12,500 s

Appendix D. Error Statistics Under Different S_T Ranges for the Other Four Experiments

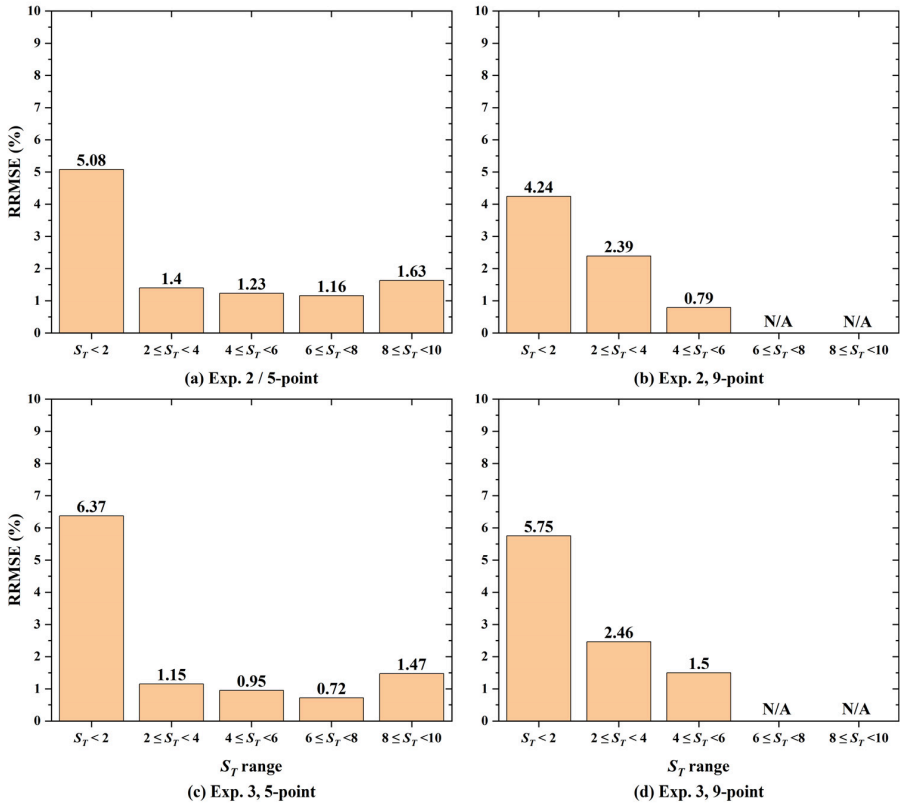


Figure A2. RRMSE statistics under different internal temperature-difference SNR (S_T) ranges for Experiments 2–3: (**a**,**b**) Experiment 2; and (**c**,**d**) Experiment 3. The left and right panels in each pair correspond to the 5-point and 9-point models, respectively.

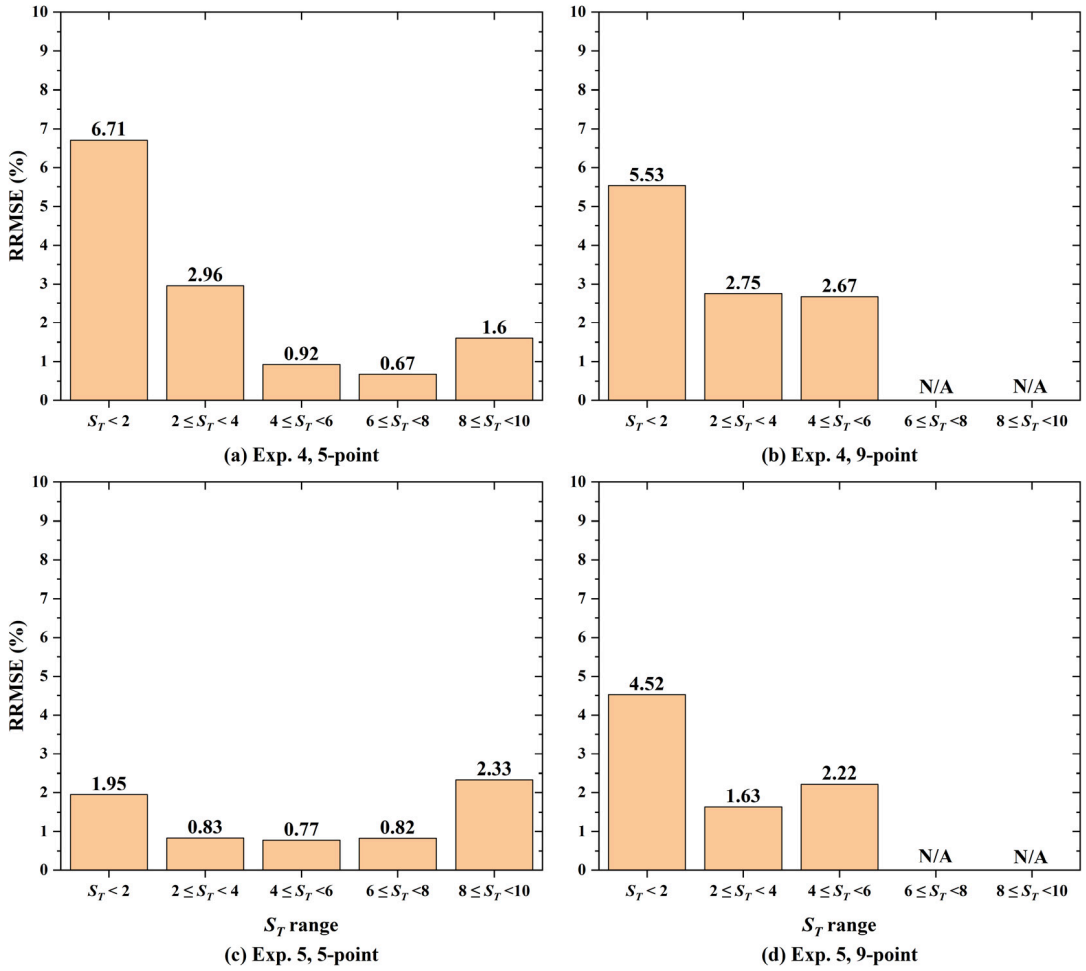


Figure A3. RRMSE statistics under different internal temperature-difference SNR (S_T) ranges for Experiments 4–5: (**a**,**b**) Experiment 4; and (**c**,**d**) Experiment 5. The left and right panels in each pair correspond to the 5-point and 9-point models, respectively.

Appendix E. Detailed Derivation of the Error-Propagation Bound for Multi-Step Virtual-Point Recursion

In Method 3, the temperature of an outer virtual point is reconstructed from adjacent inner points through the ARX-based discrete relationship. For a general recursive step, this relationship can be expressed as:

$$\widehat{T}_{i-1}(t_k) = x_1 \frac{\widehat{T}_i(t_k) - \widehat{T}_i(t_{k-1})}{\Delta t} + x_2 \widehat{T}_i(t_k) + x_3 \widehat{T}_{i+1}(t_k) \tag{A1}$$

where $\widehat{T}_{i-1}(t_k)$ is the reconstructed temperature of the current outer point, $\widehat{T}_i(t_k)$ and $\widehat{T}_i(t_{k-1})$ are the temperatures of the adjacent inner point at the current and previous time steps, respectively, and $\widehat{T}_{i+1}(t_k)$ denotes the temperature of the adjacent deeper point. The coefficients x_1, x_2, and x_3 are obtained from the ARX-identified parameter matrix. The first term represents the contribution of the transient response rate, while the second and third terms represent the contributions of the adjacent spatial temperature states.

The reconstruction error at the i-th layer is defined as:

$$e_i(t_k) = \widehat{T}_i(t_k) - T_i(t_k) \tag{A2}$$

where $T_i(t_k)$ is the corresponding true/reference temperature, and $\widehat{T}_i(t_k)$ is the reconstructed temperature. Substituting this definition into Equation (A1), the single-step error-transfer relationship can be written as:

$$e_{i-1}(t_k) = x_1 \frac{e_i(t_k) - e_i(t_{k-1})}{\Delta t} + x_2 e_i(t_k) + x_3 e_{i+1}(t_k) + \varepsilon_i(t_k) \tag{A3}$$

where $\varepsilon_i(t_k)$ represents the additional error introduced in the i-th recursive step. This term includes the ARX parameter-identification deviation, measurement noise, spatial-consistency deviation between adjacent sub-regions, finite-difference truncation error, and numerical perturbations under low-gradient conditions.

Taking the time-domain infinity norm:

$$\|e_i\|_\infty = \max_k |e_i(t_k)| \tag{A4}$$

the finite-difference error term satisfies:

$$\left\| \frac{e_i(t_k) - e_i(t_{k-1})}{\Delta t} \right\|_\infty \leq \frac{2}{\Delta t} \|e_i\|_\infty \tag{A5}$$

Therefore, the single-step error-transfer relationship can be bounded as:

$$\|e_{i-1}\|_\infty \leq \left(\frac{2|x_1|}{\Delta t} + |x_2| \right) \|e_i\|_\infty + |x_3| \|e_{i+1}\|_\infty + \|\varepsilon_i\|_\infty \tag{A6}$$

For simplicity, the combined influence of the ARX coefficients, time-difference operation, adjacent spatial term, and local recursive mapping is represented by an effective error-amplification factor G_i. Thus, Equation (A6) can be written in the compact form:

$$\|e_{i-1}\|_\infty \leq G_i \|e_i\|_\infty + \|\varepsilon_i\|_\infty \tag{A7}$$

where G_i denotes the effective error-amplification factor of the i-th recursive step. It should be noted that G_i is not introduced as a fixed material parameter, but as an upper-bound representation of the local error propagation effect during virtual-point recursion.

For an m-step virtual-point recursion process, repeated application of Equation (A7) yields:

$$\|e_0\|_\infty \leq \left(\prod_{i=1}^{m} G_i \right) \|e_m\|_\infty + \sum_{j=1}^{m} \left(\prod_{i=1}^{j-1} G_i \right) \|\varepsilon_j\|_\infty \tag{A8}$$

where e_0 is the final near-surface reconstruction error, and e_m is the error propagated from the deepest physical measurement region. Equation (A8) indicates that the final reconstruction error consists of two parts: the propagated deepest-layer error and the accumulated additional errors introduced during recursive extrapolation.

If the single-step amplification factors are approximately similar, $G_i \approx G$, and the additional error at each step satisfies $\|\varepsilon_i\|_\infty \leq \varepsilon$, Equation (A8) can be simplified as:

$$\|e_0\|_\infty \leq G^m \|e_m\|_\infty + \varepsilon \frac{G^m - 1}{G - 1}, G \neq 1 \tag{A9}$$

When $G \approx 1$, the accumulated error becomes approximately:

$$\|e_0\|_\infty \leq \|e_m\|_\infty + m\varepsilon \tag{A10}$$

Equations (A8)–(A10) show that the reconstruction error in Method 3 is governed by the recursion depth m, the single-step amplification factor, and the additional error introduced during recursive extrapolation.

In the general form of Equation (A8), the error accumulation is controlled by the step-dependent factors G_i and ε_i. Under the simplified assumptions $G_i \approx G$ and $\|\varepsilon_i\|_\infty \leq \varepsilon$, Equations (A9) and (A10) indicate that the accumulated error is mainly determined by m, G, and the upper bound ε. When G is close to unity, the error accumulates approximately linearly with the number of recursive steps. When $G > 1$, the error may increase more rapidly. This provides a quantitative explanation for the increase in reconstruction error when the measurement zone ratio d decreases and more virtual points are introduced between the physical measurement region and the target point.

Appendix F. Comparison Between Ordinary Least Squares and Tikhonov-Regularized Results for the Five Experimental Cases

Table A4. Comparison of matrix conditioning and reconstruction-error metrics obtained using ordinary least squares and Tikhonov-regularized least squares for the five experimental cases.

Case	Selection Criterion	Method	λ_0	Cond. Number	Full-Domain RRMSE/%	RRMSE S_T < 2/%	MaxRE S_T < 2/%
Exp. 1	peak	Ordinary LS	0	6.04×10^7	4.27	7.25	22.02
Exp. 1	peak	Tikhonov LS	3.00×10^{-9}	5.70×10^7	4.39	7.31	20.99
Exp. 2	peak	Ordinary LS	0	7.11×10^7	2.72	4.24	66.43
Exp. 2	peak	Tikhonov LS	3.00×10^{-10}	7.06×10^7	2.85	4.40	66.13
Exp. 3	lowST	Ordinary LS	0	7.02×10^7	3.87	5.75	84.12
Exp. 3	lowST	Tikhonov LS	3.00×10^{-9}	6.56×10^7	3.43	5.49	77.21
Exp. 4	peak	Ordinary LS	0	1.00×10^8	3.64	5.53	18.63
Exp. 4	peak	Tikhonov LS	0	1.00×10^8	3.64	5.53	18.63
Exp. 5	lowST/peak	Ordinary LS	0	6.31×10^7	3.00	4.52	26.71
Exp. 5	lowST/peak	Tikhonov LS	1.00×10^{-9}	6.18×10^7	3.13	4.43	25.23

Appendix G. Full-Column Rank Verification of the Experimental ARX Regression Matrices

To verify the uniqueness condition of the finite-dimensional least squares parameter identification in Equation (9), the regression matrices $\mathbf{B}$ were constructed from the complete temperature sequences of the five experimental datasets for both the 5-point and 9-point models. Each regression matrix contains three columns corresponding to the three equivalent ARX parameters; therefore, the number of parameters to be identified is $n_X = 3$.

For the linear least squares problem $\mathbf{A} = \mathbf{BX}$, the parameter solution is unique when the regression matrix satisfies $\mathrm{rank}(\mathbf{B}) = n_X$, because $\mathbf{B}^{\mathrm{T}}\mathbf{B}$ is then nonsingular.

The numerical rank was calculated directly from the original regression matrix $\mathbf{B}$. In addition, because the columns of $\mathbf{B}$ have different numerical scales, each column was normalized to the unit Euclidean norm before calculating the minimum singular value. The resulting column-normalized matrix is denoted as $\mathbf{B}_{\mathrm{norm}}$. Since column normalization only multiplies $\mathbf{B}$ by a nonsingular diagonal scaling matrix, it does not change the matrix rank.

The numerical results are summarized in Table A5. All ten original regression matrices have a rank of three, equal to the number of identified parameters. Moreover, the minimum singular values of the corresponding normalized matrices, $\sigma_{\min}(\mathbf{B}_{\mathrm{norm}})$, are greater than zero. Therefore, all regression matrices satisfy the full-column rank condition, confirming that the least squares parameter solution is unique for the experimental datasets considered in this study.

Table A5. Numerical full-column rank verification of the ARX regression matrices constructed from the five experimental datasets.

Dataset	Model	Matrix Size	Rank(B)	$\sigma_{\min}(\mathbf{B}_{\mathbf{norm}})$	Full Column Rank
Exp. 1	5-point	15,892 × 3	3	0.013568	Yes
Exp. 2	5-point	13,071 × 3	3	0.017855	Yes
Exp. 3	5-point	17,716 × 3	3	0.016795	Yes
Exp. 4	5-point	22,428 × 3	3	0.016141	Yes
Exp. 5	5-point	12,784 × 3	3	0.018565	Yes
Exp. 1	9-point	15,892 × 3	3	0.005748	Yes
Exp. 2	9-point	13,071 × 3	3	0.007062	Yes
Exp. 3	9-point	17,716 × 3	3	0.006978	Yes
Exp. 4	9-point	22,428 × 3	3	0.006579	Yes
Exp. 5	9-point	12,784 × 3	3	0.007533	Yes

References

1. Brevault, L.; Balesdent, M.; Hebbal, A. Multi-objective multidisciplinary design optimization approach for partially reusable launch vehicle design. *J. Spacecr. Rockets* **2020**, *57*, 373–390. [CrossRef]
2. Bauer, W.; Rickmers, P.; Kallenbach, A.; Stappert, S.; Wartemann, V.; Merrem, C.H.J.; Schwarz, R.; Sagliano, M.; Grundmann, J.T.; Flock, A.; et al. DLR reusability flight experiment ReFEx. *Acta Astronaut.* **2020**, *168*, 57–68. [CrossRef]
3. Balesdent, M.; Brevault, L.; Paluch, B.; Thépot, R.; Wuilbercq, R.; Subra, N.; Defoort, S.; Bourgaie, M.; Vieille, B. Multidisciplinary design and optimization of winged architectures for reusable launch vehicles. *Acta Astronaut.* **2023**, *211*, 97–115. [CrossRef]
4. Wang, K.; Wang, J.; Liu, Z.; Zhang, S.; Zhang, B.; Quan, W. Thermal modal analysis of hypersonic composite wing on transient aerodynamic heating. *Sci. Rep.* **2024**, *14*, 11012. [CrossRef] [PubMed]
5. He, L.; Chen, F.; Qin, Y. A novel data-driven method for predicting heat flux of hypersonic aircraft based on Fourier neural operator. *Aerosp. Sci. Technol.* **2026**, *169*, 111397. [CrossRef]
6. Ye, J.; Zhang, M.; Zhang, Y.; Zhu, J.; Li, Q. Numerical modeling and optimization of active heat dissipation in honeycomb sandwich microchannels for aircraft applications. *Case Stud. Therm. Eng.* **2025**, *74*, 106869. [CrossRef]
7. Yang, C.; Pu, H.; Mu, L.; Zhou, L.; Bao, J.; Zhang, Y.; Dong, M. Multi-objective synergistic optimization of closed Brayton cycle superstructure for thermal protection system of high-Mach-number air-breathing vehicles. *Case Stud. Therm. Eng.* **2025**, *73*, 106556. [CrossRef]
8. Alifanov, O.M.; Salosina, M.O.; Budnik, S.A.; Nenarokomov, A.V. Design of aerospace vehicles' thermal protection based on heat-insulating materials with optimal structure. *Aerospace* **2023**, *10*, 629. [CrossRef]
9. Le, V.T.; Ha, N.S.; Goo, N.S. Advanced sandwich structures for thermal protection systems in hypersonic vehicles: A review. *Compos. Part B Eng.* **2021**, *226*, 109301. [CrossRef]
10. Chen, Z.; Zhang, K.; Zhao, S.; Li, F.; Xu, F.; Chen, M. Probabilistic design method for aircraft thermal protective layers based on surrogate models. *Energies* **2024**, *17*, 1051. [CrossRef]
11. Li, C.; Li, X.; Chen, J.; Liang, X.; Yu, L.; Ai, F.; Yuan, C.; Cao, H. Optimization design of thermal protective characteristics of special-shaped honeycomb structure. *Case Stud. Therm. Eng.* **2024**, *60*, 104657. [CrossRef]
12. Han, G.; Yang, Q.; Yang, F.; Xie, W.; Jin, H.; Yi, F.; Meng, S.; Peng, Z. Design and efficiency assessment of hybrid thermal protection structures for return capsule reentry. *Case Stud. Therm. Eng.* **2023**, *41*, 102656. [CrossRef]
13. Woodbury, K.A.; Najafi, H.; De Monte, F.; Beck, J.V. *Inverse Heat Conduction: Ill-Posed Problems*, 2nd ed.; John Wiley & Sons: Hoboken, NJ, USA, 2023.
14. Ciofalo, M. Solution of an inverse heat conduction problem with third-type boundary conditions. *Int. J. Therm. Sci.* **2022**, *175*, 107466. [CrossRef]
15. Orlande, H.R.B. *Inverse Heat Transfer: Fundamentals and Applications*; CRC Press: Boca Raton, FL, USA, 2021. [CrossRef]
16. Zhou, L.; Zhang, C.; Bai, Y.; Liu, K.; Cui, M. Improved particle swarm optimization for solving transient nonlinear inverse heat conduction problem in complex structure. *Trans. Nanjing Univ. Aeronaut. Astronaut.* **2021**, *38*, 816. [CrossRef]
17. Zhou, L.; Lv, J.; Cui, M.; Peng, H.; Gao, X. A polygonal element differential method for solving two-dimensional transient nonlinear heat conduction problems. *Eng. Anal. Bound. Elem.* **2023**, *146*, 448–459. [CrossRef]

18. Pandey, V.; Bekele, A.; Ahmed, G.M.S.; Kanu, N.J.; Singh, G.K. An application of conjugate gradient technique for determination of thermal conductivity as an inverse engineering problem. *Mater. Today Proc.* **2021**, *47*, 3082–3087. [CrossRef]
19. Cui, M.; Mei, J.; Zhang, B.W.; Xu, B.B.; Zhou, L.; Zhang, Y. Inverse identification of boundary conditions in a scramjet combustor with a regenerative cooling system. *Appl. Therm. Eng.* **2018**, *134*, 555–563. [CrossRef]
20. Khosravi, M.; Mohammadiun, M.; Mohammadiun, H. Solving an inverse problem with four unknown boundary conditions in a lid-driven cavity with heated walls using the Levenberg–Marquardt method. *Appl. Eng. Sci.* **2025**, *23*, 100245. [CrossRef]
21. Sajedi, R.; Faraji, J.; Kowsary, F. A new damping strategy of Levenberg–Marquardt algorithm with a fuzzy method for inverse heat transfer problem parameter estimation. *Int. Commun. Heat Mass Transf.* **2021**, *126*, 105433. [CrossRef]
22. Khan, A.I.; Billah, M.M.; Ying, C.; Liu, J.; Dutta, P. Bayesian method for parameter estimation in transient heat transfer problem. *Int. J. Heat Mass Transf.* **2021**, *166*, 120746. [CrossRef]
23. Wang, X.; Zhang, D.; Zhang, L. Estimation of moving heat source for an instantaneous three-dimensional heat transfer system based on step-renewed Kalman filter. *Int. J. Heat Mass Transf.* **2020**, *163*, 120435. [CrossRef]
24. Wei, X.; Nan, P.; Xin, G.; Zhang, Y.; Yang, H. Efficient real-time reconstruction of transient temperature fields in some hypersonic thermal protection systems with a conditioned adaptive physics network. *Aerosp. Sci. Technol.* **2026**, *168*, 111320. [CrossRef]
25. Wei, X.; Jin, K.; Nan, P.; Zhou, F.; Xin, G.; Lim, K.-S.; Ahmad, H.; Zhang, Y.; Yang, H. Global rapid thermomechanical decoupling method based on adaptive localized method of fundamental solutions and sparse embedded FBG in thermal protection materials for aerospace vehicles. *Int. J. Therm. Sci.* **2025**, *218*, 110166. [CrossRef]
26. Zhang, B.; Wu, G.; Gu, Y.; Wang, X.; Wang, F. Multi-domain physics-informed neural network for solving forward and inverse problems of steady-state heat conduction in multilayer media. *Phys. Fluids* **2022**, *34*, 116116. [CrossRef]
27. He, Z.; Ni, F.; Wang, W.; Zhang, J. A physics-informed deep learning method for solving direct and inverse heat conduction problems of materials. *Mater. Today Commun.* **2021**, *28*, 102719. [CrossRef]
28. Billah, M.M.; Khan, A.I.; Liu, J.; Dutta, P. Physics-informed deep neural network for inverse heat transfer problems in materials. *Mater. Today Commun.* **2023**, *35*, 106336. [CrossRef]
29. Shang, Y.; Tan, C.; Yu, X.; Hu, X.; Jiang, H.; Ma, W.; Liu, D. Using neural networks: A guidance with application in inverse heat conduction problem. *Eur. J. Phys.* **2025**, *46*, 025102. [CrossRef]
30. Zhou, C.; Li, T.; Lan, C.; Du, R.; Xin, G.; Nan, P.; Yang, H.; Wang, G.; Liu, X.; Li, W. Physics-informed neural networks with complementary soft and hard constraints for solving complex boundary Navier–Stokes equations. *arXiv* **2024**, arXiv:2411.08122. [CrossRef]
31. Liu, Y.; Zhou, C.; Xin, G.; Nan, P.; Yang, H. A cooperative soft-hard PINN framework for decoupling the thermoelasticity and thermal convection multiphysics. *Appl. Sci.* **2026**, *16*, 1885. [CrossRef]
32. Slagel, J.T.; Chung, J.; Chung, M.; Kozak, D.; Tenorio, L. Sampled Tikhonov regularization for large linear inverse problems. *Inverse Probl.* **2019**, *35*, 114008. [CrossRef]
33. Calvetti, D.; Somersalo, E. Inverse problems: From regularization to Bayesian inference. *WIREs Comput. Stat.* **2018**, *10*, e1427. [CrossRef]
34. Shahnazari, M.R.; RoohiShali, A.; Saberi, A. Solving inverse heat conduction problems by using Tikhonov regularization in combination with the genetic algorithm. *Int. J. Appl. Math. Comput. Sci. Syst. Eng.* **2021**, *3*, 60–66.
35. Tourn, B.A.; Hostos, J.C.A.; Fachinotti, V.D. Implementation of total variation regularization-based approaches in the solution of linear inverse heat conduction problems concerning the estimation of surface heat fluxes. *Int. Commun. Heat Mass Transf.* **2021**, *125*, 105330. [CrossRef]
36. Loussouarn, T.; Maillet, D.; Remy, B.; Schick, V.; Dan, D. Indirect measurement of temperature inside a furnace, ARX model identification. *J. Phys. Conf. Ser.* **2018**, *1047*, 012006. [CrossRef]
37. Zawada-Tomkiewicz, A.; Tomkiewicz, D.; Pela, M. Identification of a workpiece temperature compensation model for automatic correction of the cutting process. *Materials* **2022**, *15*, 8372. [CrossRef] [PubMed]
38. Oliveira, A.V.S.; Avrit, A.; Gradeck, M. Thermocouple response time estimation and temperature signal correction for an accurate heat flux calculation in inverse heat conduction problems. *Int. J. Heat Mass Transf.* **2022**, *185*, 122398. [CrossRef]
39. Zhao, X.; Jin, K.; Yan, M.; Nan, P.; Zhou, F.; Xin, G.; Lim, K.S.; Ahmad, H.; Zhang, Y.; Yang, H. Inverse heat transfer for real-time thermal evaluation of aircraft thermal protection structure with embedded FBG sensors. *Appl. Therm. Eng.* **2025**, *260*, 124869. [CrossRef]
40. Liu, Y.; Zhao, X.; Wei, X.; Nan, P.; Zhou, F.; Xin, G.; Lim, K.S.; Zhang, Y.; Yang, H. Real-time sensor for measuring the surface temperature of thermal protection structures based on the full-time domain temperature inversion method. *Sensors* **2025**, *25*, 2227. [CrossRef] [PubMed]
41. Delcroix, B.; Le Ny, J.; Bernier, M.; Azam, M.; Qu, B.; Venne, J.S. Autoregressive neural networks with exogenous variables for indoor temperature prediction in buildings. *Build. Simul.* **2021**, *14*, 165–178. [CrossRef]
42. Brociek, R.; Hetmaniok, E.; Napoli, C.; Capizzi, G.; Słota, D. Reconstruction of aerothermal heating for the thermal protection system of a reusable launch vehicle. *Appl. Therm. Eng.* **2023**, *219*, 119405. [CrossRef]

43. Ferraiuolo, M.; Manca, O. Heat transfer in a multi-layered thermal protection system under aerodynamic heating. *Int. J. Therm. Sci.* **2012**, *53*, 56–70. [CrossRef]
44. Kakaç, S.; Yener, Y.; Naveira-Cotta, C.P. *Heat Conduction*, 5th ed.; CRC Press: Boca Raton, FL, USA, 2018. [CrossRef]

Disclaimer/Publisher's Note: The statements, opinions and data contained in all publications are solely those of the individual author(s) and contributor(s) and not of MDPI and/or the editor(s). MDPI and/or the editor(s) disclaim responsibility for any injury to people or property resulting from any ideas, methods, instructions or products referred to in the content.